Rydberg atoms in low-frequency fields

Fundamental aspects and applications

Rydberg atoms in low-frequency fields

Fundamental aspects and applications

EEN WETENSCHAPPELIJKE PROEVE OP HET GEBIED VAN
DE NATUURWETENSCHAPPEN, WISKUNDE EN INFORMATICA

PROEFSCHRIFT

ter verkrijging van de graad van doctor
aan de Katholieke Universiteit van Nijmegen
op gezag van de Rector Magnificus Prof. dr C. W. P. M. Blom
in het openbaar te verdedigen op maandag 15 december 2003
des namiddags om 15:00 uur precies
door

Andreas Stefan Gürtler

geboren op 8 augustus 1972
te Waibstadt, Duitsland

Promotor	Prof. dr W. J. van der Zande
Copromotor	Prof. dr L. D. Noordam
Manuscript commissie	Prof. dr T. Rasing Prof. dr H. B. van Linden van den Heuvell PD Dr P. U. Jepsen

ISBN: 90-77209-04-2

The work described in this thesis was performed at the

FOM Instituut voor Atoom- en Molecuulfysica (AMOLF)
Kruislaan 407
1098SJ Amsterdam
www.amolf.nl

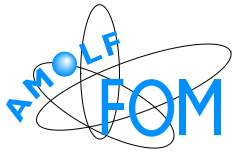

This work is part of the research program of the Stiching voor Fundamenteel Onderzoek der Materie (FOM) and was financially supported by the Nederlandse Organisatie voor Wetenschappelijk Onderzoek (NWO) and by the European Community's Human Potential Programme under contract HPRN-CT-1999-00129, COCOMO.

für meine Eltern
for Laura

List of publications to which the author contributed:

A. Gürtler, A. S. Meijer and W. J. van der Zande, *Transitions driven by an absorbed frequency*. In preparation for Physical Review Letters (Chapter 6 of this thesis)

A. Gürtler, L. D. Noordam and W. J. van der Zande, *State-selective field ionization of rubidium*. Submitted to Phys. Lett. A (Chapter 4 of this thesis)

A. Gürtler, W. J. van der Zande and L. D. Noordam, *Asymmetry in the ionization of Rydberg atoms by few-cycle radiofrequency pulses.* Submitted to Phys. Rev. Lett. (Chapter 3)

A. Gürtler, M. J. J. Vrakking, W. J. van der Zande and L. D. Noordam, *Carrier-phase dependence in the ionization of Rydberg atoms by short radiofrequency pulses, a model system for high order harmonic generation.* Submitted to Phys. Rev. Lett. (Chapter 2 of this thesis)

A. Gürtler, A. S. Meijer and W. J van der Zande, *Imaging of terahertz radiation using a Rydberg atom photocathode.* Appl. Phys. Lett. **83**, 222 (2003) (Chapter 5 of this thesis)

A. Wetzels, A. Gürtler, A. Buijserd, T. Vijftigschild, H. ter Horst and W. J. van der Zande, *Reduction of electronic noise in THz generation.* Rev. Sci. Inst. **74**, 3180 (2003)

A. Wetzels, A. Gürtler, F. Roşca-Prună, S. Zamith, M. J. J. Vrakking F. Robicheaux and W. J. van der Zande, *Two-dimensional momentum imaging of Rydberg state*s *using half-cycle pulse ionization and velocity-map imaging.* Phys. Rev. A **68**, 041401(R) (2003)

A. Wetzels, A. Gürtler, L. D. Noordam, F. Robicheaux, C. Dinu, H. G. Muller, M. J. J. Vrakking, W. J. van der Zande, *Rydberg state ionization by half-cycle pulse excitation: Strong kicks create slow electrons*. Phys. Rev. Lett. 89, 273003 (2002)

J. B. M. Warntjes, A. Gürtler, A. Osterwalder, F. Roşca-Prună, M. J. J. Vrakking and L. D. Noordam, *Atomic streak camera operating in the extreme ultraviolet.* Rev. Sci. Inst. **72**, 3205 (2001)

J. B. M. Warntjes, A. Gürtler, A. Osterwalder, F. Roşca-Prună, M. J. J. Vrakking and L. D. Noordam *Atomic spectral detection of tunable extreme ultraviolet pulses.* Opt. Lett **26**, 1463 (2001)

A. A. R. Wetzels, A. Gürtler, H. G. Muller and L. D. Noordam, *The dynamics of a THz Rydberg wavepacket.* Eur. Phys. J. D **14**, 157 (2001)

A. Gürtler, C. Winnewisser, H. Helm and P. U. Jepsen, *Terahertz pulse propagation in the near field and the far field.* J. Opt. Soc. Am. A **17**, 74 (2000)

Contents

Preface

Atoms in highly excited electronic states - Rydberg atoms - are an extremely useful tool to gain insight in atomic dynamics. The understanding of stationary Rydberg states has progressed tremendously in the last decades [29, 79][1]. The typical length- and time scales of Rydberg atoms scale as the square and third power of the principal quantum number n, respectively, bringing these values into regions which are accessible by modern ultrafast laser technology. The last decade has seen extensive investigations into time-dependent coherent superpositions of Rydberg wavefunctions, so-called wavepackets [63]. Although exact numerical predictions of experiments on high Rydberg states are often hampered by the huge spatial extent of Rydberg wavefunctions as well as the long time scales and the large number of states involved in many experiments, the principal understanding of Rydberg atoms has been accomplished. Experimentally, the development in laser technology has not only greatly simplified many experiments, but has also led to a high degree of control over the Rydberg wavefunction [91]. Together, advances in theoretical and experimental techniques have led to the development of schemes using Rydberg states of atoms as detectors for far-infrared radiation [24, 30], photocathodes for imaging and streak cameras in the infrared [22, 23] and Rydberg atom data registers [2]. The applications extend to fields as diverse as characterization of electric fields in glow discharges [16] and the search for elusive cosmic dark-matter particles, the axions [10].

In this thesis, we investigate high Rydberg states in low-frequency fields. The outline of the thesis is as follows: Chapter 1 gives a brief introduction on Rydberg atoms. In chapter 2 we use the long time scales of Rydberg orbits and the sensitivity of Rydberg states to electric fields to establish a connection between radiofrequency ionization of high Rydberg states and high order harmonic generation using ground-state atoms and few-cycle laser pulses. The strong interaction of few-cycle radiofrequency fields with high Rydberg states gives rise to asymmetries in the ionization process, and such phenomena are investigated as a function of radiofrequency field strength, carrier-envelope phase and pulse duration in chapter 3. In chapter 4 we demonstrate a refined field ionization technique to detect the state distribution of a Rydberg atom population based on shaped field ramps. In chapter 5 an imaging camera

[1] In this thesis, the citations in the bibliography are sorted alphabetically by the first author's surname rather than in order of appearance.

for far-infrared electromagnetic pulses, called THz pulses after their frequency spectrum, is presented. THz pulses display complex interactions with Rydberg states. A delicate feature of this interaction is used in chapter 6 to measure an absorption line of gaseous water.

Chapter 1

Rydberg atoms - A brief introduction

In this chapter we introduce some of the well-known basics of Rydberg atom physics which are indispensible for the understanding of Rydberg atom experiments. Extensive reviews of many aspects of the physics of highly excited atoms and molecules are given in Refs. [29, 79]. Non-stationary Rydberg states are discussed in detail in Ref. [63].

In section 1.2 we develop an intuitive understanding by describing the Rydberg atom using the semi-classical Bohr-Sommerfeld model. This view of highly excited states is often helpful to understand the general properties, scaling laws and dynamics of Rydberg states. In section 1.3, we briefly outline a more quantitative way of treating Rydberg atoms, the integration of the stationary Schrödinger equation. This method is then applied in the following sections to calculate the energy levels of Rydberg states in external electric and magnetic fields, so-called Stark and Zeeman states. Stark states are used frequently throughout this thesis, e. g. in chapter 4 to explain the path of a Rydberg state from zero field to the ionization limit and in chapter 6 to Stark-tune the energy difference between adjacent Rydberg levels. In chapters 5 and 6 of this thesis far-infrared half-cycle field pulses in the THz frequency regime are used. The interaction of these pulses with Rydberg states is outlined in section 1.5. The ionization of diamagnetic Zeeman states by ultrashort electromagnetic half-cycle pulses is used in section 1.6 as an example for the classical model of Rydberg atoms and the special interaction of Rydberg states with half-cycle radiation.

1.1 Atomic units

In atomic and molecular physics it is often convenient to use the atomic unit system introduced by Hartree [41]. In this unit system, quantities are measured relative to ground state atomic hydrogen and $e\ (\text{electron charge}) = 1,\ \hbar\ (\text{Planck action}) = 1,\ M_e\ (\text{electron mass}) = 1$. Table 1.1 lists the most common atomic units and their equivalents in SI units along with a few other useful unit conversions. Throughout this thesis, atomic units (a. u.) are used unless other units are given explicitly.

Table 1.1: Frequently used unit conversions (source: Ref. [61]) .

		SI	alternative
distance	1 a. u. =	$5.291\,772 \cdot 10^{-11}$ m	0.53 Å
time	1 a. u. =	$2.418\,884 \cdot 10^{-17}$ s	24.2 as
frequency	1 a. u. =	$4.134\,137 \cdot 10^{16}$ Hz	
energy	1 a. u. =	$4.359\,743 \cdot 10^{-18}$ J	27.21 eV
			$6.5797 \cdot 10^{15}$ Hz
velocity	1 a. u. =	$2.187\,691 \cdot 10^{6}$ m/s	$c/137.036$
electric field	1 a. u. =	$5.142\,206 \cdot 10^{9}$ V/cm	
magnetic field	1 a. u. =	$2.350\,517 \cdot 10^{5}$ T[1]	
intensity	1 a. u.=	$3.51 \cdot 10^{16}$ W/cm^2	
energy	1 eV =	8065.54 cm^{-1}	1.24 μm
energy	1 cm^{-1} =	29.98 GHz	$\hat{=}$33.37 ps

[1] The atomic unit of magnetic field is defined differently (1 a. u. = 1715 T) in some references, see e. g. [48].

1.2 Semi-classical description of Rydberg atoms

The Ehrenfest principle demands that for high quantum numbers, expectation values of quantum mechanical observables obey the classical laws of motion. Therefore, the semi-classical description of a Rydberg atom as an electron circling on Kepler orbits in the $1/r$-potential of the atomic core, like a planet around the sun, is a very powerful tool in understanding the properties of Rydberg states. Indeed, once the purely classical Kepler problem is enriched with axioms from quantum mechanics, most importantly the quantization of energy and angular momentum, the resulting atomic model of Bohr and Sommerfeld describes many experiments in Rydberg atom physics with astonishing accuracy. The semi-classical model of Rydberg atoms provides an intuitive picture of Rydberg atom physics. It is, however, very important to keep in mind its limitations and the difficulties of translating the classical results into the quantum world of atoms.

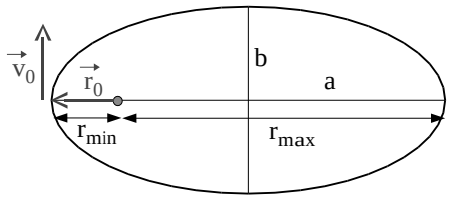

Figure 1.1: Parameters of an elliptical orbit with energy $E_n = -1/2n^2$; semi-major axis $a = n^2$ (*n* is the principal quantum number), semi-minor axis $b = (a/n) \cdot l \quad (l = 0.5, ..., n - 0.5)$. $|\vec{L}| = l$ is the angular momentum of the orbit.

Equation of motion

The equation of motion in the classical atomic model, an electron in the Coulomb field of the atomic core, is the Kepler equation (given in atomic units):

$$\ddot{\vec{r}} = -\frac{\vec{r}}{r^3}. \tag{1.1}$$

The solutions of Eq. (1.1) are ellipses with the atomic core in one focal point as depicted in Fig. 1.1. The classical equation of motion (1.1) must be combined with initial conditions derived from quantum mechanics. A stationary Rydberg state is described by the quantum numbers *n*, *l*, *m*, which give the state's energy, angular momentum and its projection on the quantization axis. The energy of the initial state $E_n = -1/(2n^2)$ (the famous Rydberg formula) determines the major axis *a* of the ellipse. The angular momentum determines the minor axis (Sommerfeld quantization condition). This leads to

$$a = n^2 \tag{1.2}$$

$$b = \frac{a}{n} l \quad , \; l = \frac{1}{2} \ldots n - \frac{1}{2} \tag{1.3}$$

To solve the equation of motion, we let the electron start at the inner turning point of the ellipse. The initial conditions for the radial coordinate r and the velocity v are then

$$|\vec{r}_0| = r_{min} = a - \sqrt{a^2 - b^2} \qquad |\vec{v}_0| = 2\sqrt{-\frac{1}{2n^2} + \frac{1}{r_{min}}} \tag{1.4}$$

For a two-dimensional description, the initial conditions are as given here. A detailed description of the integration of the equation of motion in three dimensions is given in Appendix A.

Figure 1.2 shows the orbits and the velocity distributions of some $n = 40$ states. Some observations can be made in this plot: i) The circular high-ℓ states never come near the electronic core and are thus insensitive to the exact structure of the core. ii) The low-ℓ states extend to much larger distances from the core compared to high-ℓ states. They spend most of

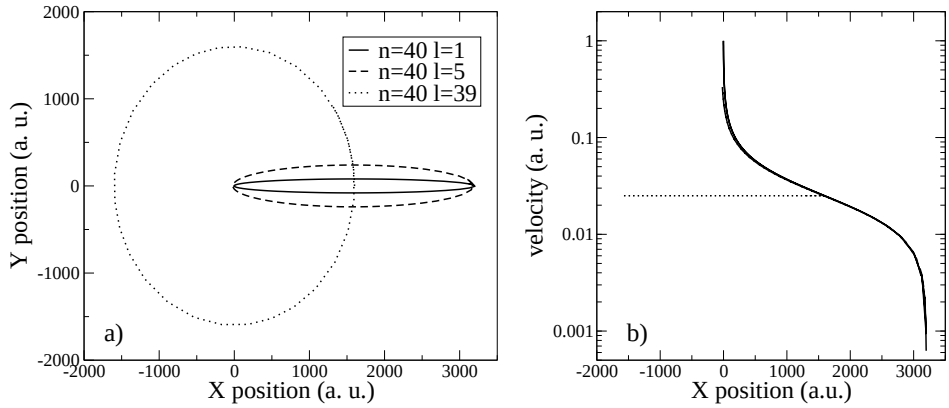

Figure 1.2: a) Classical orbits orbits of the n=40, l=1; n=40, l=5 and n=40, l=39 states. The core is at the origin. b) Absolute value of the velocity of the Rydberg electron.

their time at large r, as the velocity far away from the core is very low. The velocity changes three orders of magnitude for the depicted n=40, $\ell = 1$ state.

Properties of Rydberg atoms - a classical intuition

Many well-known properties and scaling laws of Rydberg atoms can be understood by this classical model. It can provide valuable intuitive insight into Rydberg states and their interaction with light and external fields.

- The **scaling law for the orbit time** T_K of a Rydberg state, $T_K \propto n^3$, follows directly from Kepler's Third Law, T_K^2/a^3 =const., as the semi-major axis a is proportional to n^2.
- The **low photoionization cross section** can be explained by the fact that the electron spends most of its orbit time far away from the core, where it is almost free. A multicycle laser pulse can not transfer energy to a free electron, as it only "quivers" in the laser field without net energy change. Only during the short time it spends near the core is the Rydberg electron susceptible to the laser pulse, as it is bent around by the core such that, in the best case, it turns around exactly at a zero-crossing of the laser field, thus gaining energy from the positive as well as the negative field components. The time the electron spends near the core is nearly independent of n, while the roundtrip time scales like n^3. This leads to an n^{-3} scaling in the photoionization cross section. The same reasoning explains the n^{-3} scaling of the **photoexcitation cross section** of a Rydberg state with principal quantum number *n*.

- The same fact explains the **long lifetime** of high Rydberg states as radiative decay, i. e. the emission of a photon can also only occur near the core.
- The orbits of low-ℓ states come close enough to the core to penetrate the electron shells of non-hydrogenic atoms. This leads to **core scattering** and **quantum defects**, i. e. suppression of energy levels, of low-ℓ states, which become more important for heavier atoms.
- The energy spacing between two neighboring Rydberg states n and $n+1$, which is n^{-3} in atomic units, is the reason for the extremely **high cross sections for $\mathbf{n \rightarrow n+1}$ transitions** in Rydberg atoms. Because of the n^3 scaling of the orbit time, an external frequency of $(n^{-3}/2\pi) \cdot 4.13 \times 10^{16}$ Hz is exactly in phase with the Rydberg orbit, so the Rydberg electron gains energy throughout the optical cycle.

All of these properties are frequently used in Rydberg experiments, and many of them will be found in this thesis. The intuitive classical picture is an extremely valuable tool to predict outcomes and interpret results of Rydberg experiments, although one should always keep in mind the quantum nature of atomic systems and the limitations of the classical model.

1.3 Quantum mechanical description of Rydberg Atoms

For many aspects of Rydberg atoms, most notably the term energies, a quantum mechanical description is required. For hydrogen, the time-independent Schrödinger equation reads

$$\left(-\frac{\nabla^2}{2} - \frac{1}{r}\right) \cdot \psi = E \cdot \psi \tag{1.5}$$

which can be separated into an angular and a radial part and solved analytically to give the well-known solutions [9]

$$\psi^H_{nlm}(\theta, \phi, r) = Y_{lm}(\theta, \phi) \cdot \frac{f(E_n, l, r)}{r} \tag{1.6}$$

with Eigenvalues

$$E_n = -\frac{1}{2n^2} \tag{1.7}$$

where the Y_{lm} are the spherical harmonics and $f(E, l, r)$ are the regular Coulomb functions. The energy of a hydrogenic Rydberg state depends only on n, such that states with equal n but different ℓ are degenerate.

In this thesis alkali metal atoms, namely rubidium, have been used. For Rydberg states of non-hydrogenic atoms, the energy of a state $|n, l\rangle$ is, in first order, given by the Rydberg formula

$$E_n = -\frac{1}{2(n-\delta_\ell)^2} \tag{1.8}$$

with the quantum defect δ_ℓ which depends on the angular momentum ℓ. The interaction of the low angular momentum states with the electronic core suppresses the energy levels of low-ℓ states with respect to their hydrogenic counterparts. An alkali-metal Rydberg state can in good approximation be described by the single-particle Hamiltonian

$$\mathcal{H} = -\frac{\nabla^2}{2} + V(r) \tag{1.9}$$

where $V(r) \approx 1/r$ for large r. $V(r)$ can include fine-structure as well as core-polarization terms. For many practical purposes, where the part of the wavefunction far away from the core is strongly weighted, it is not necessary to know the form of $V(r)$. Wavefunctions ψ_{nlm} with the correct Eigenenergies can be obtained by numerically integrating the radial Schrödinger equation with a cutoff at small *r*, using quantum defects, i. e. Eigenenergies, of the low-ℓ states known from spectroscopy [105]. The resulting wavefunctions are phase-shifted compared to the hydrogenic Eigenfunctions by δ_ℓ/π [29].

The precise experimental quantum defects of rubidium used in this thesis are taken from Ref. [54]. Very recently, the accuracy of Rb quantum defects was improved by an order of magnitude [53]. The matrix elements for the Stark operator r as well as the diamagnetic operator r^2, which are of paramount importance in this thesis, can be evaluated in this way [104, 105]. In section 1.4 the wavefunctions ψ_{nlm} will be used to calculate the energy levels of Rydberg atoms in external electric and magnetic fields.

1.4 Rydberg atoms in external fields

1.4.1 Electric fields

The effect of an electric field on a Rydberg atom is twofold: it lifts the degeneracy of the Eigenstates with the same principal quantum number n but different angular momentum ℓ and it introduces a saddle point to the Coulomb potential, which lowers the ionization barrier. The combined Coulomb and electric field potential $V(r) = -1/r + F \cdot x$ is shown in Fig. 1.3.

In hydrogen, ℓ-states of the principal quantum number n are degenerate. In non-hydrogenic atoms, only the high-ℓ states are degenerate in zero field, the low-ℓ states are suppressed in energy by their interaction with the core. An external electric field lifts this degeneracy and the resulting states $|n,k\rangle = \sum_\ell c_\ell |n,\ell\rangle$, called Stark states, are linear combinations of the zero-field eigenstates $|n,\ell\rangle$ of the angular momentum operator. k denotes the dipole moment of the state and lies in the range of $-n+1+|m|, \ldots, n-1-|m|$ in steps of 2. In hydrogen, the energy of a state $|n,k\rangle$ is, in first order, given by

$$E_{n,k} = -\frac{1}{2n^2} + \frac{3}{2} \cdot n \cdot k \cdot F \tag{1.10}$$

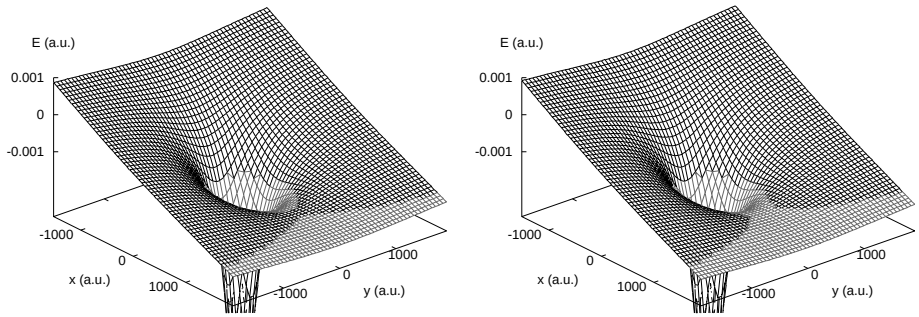

Figure 1.3: Combined potential of a Coulomb field and an external electric field F . The light lines denote points where the potential energy is smaller than the energy of a state bound by $403\,\mathrm{cm}^{-1}$, i. e. the classically allowed region for a state with $E = -403\,\mathrm{cm}^{-1}$. The saddle point in positive *x*-direction is clearly seen. (a) $F = 4320$ V/cm. The saddle point lies around $-402\,\mathrm{cm}^{-1}$. The bound state can ionize only by tunneling. (b) $F = 4500\,\mathrm{V/cm}$. The saddle point lies around $-411\,\mathrm{cm}^{-1}$. The state is classically free to leave the atom over the saddle point and ionize.

where F denotes the electric field. States which gain energy in the field (*k*>0) are called "blue" Stark states, while states which lose energy (*k*<0) are called "red" Stark states. In fields higher than the *Inglis-Teller limit*

$$F_{IT} = \frac{1}{3n^5}, \tag{1.11}$$

the so-called *n-mixing regime* is reached, in which states of adjacent n manifolds mix.

In a ground-state atom, the Coulomb field amounts to many GV/cm, such that static laboratory fields are small compared to the atomic fields and only the strong AC fields produced by short pulsed lasers can reach these field strengths. In highly excited atoms on the other hand, the Rydberg electron spends most of its time far away from the core, where the Coulomb force binding it to the core is weak. An external electric field F introduces a saddle point to the Coulomb potential (see Fig. 1.3) with an energy

$$E_c = 2 \cdot \sqrt{F}. \tag{1.12}$$

States with energies above this value are classically unbound (Fig. 1.3b). States which lie below the saddle point energy can ionize by tunneling (Fig. 1.3a). However, this is only true for non-hydrogenic atoms. The "blue" Stark states are localized on the "uphill" side of the core (negative *x* in Fig. 1.3) such that the wavefunction never probes the saddle point region

at positive *x*. In a pure Coulomb potential, this blue character (i. e. the dipole moment k) is conserved and blue states ionize at much higher fields than expected from Eq. (1.10) and (1.12). A non-hydrogenic core introduces a coupling to the "red" states. If we combine Eq. (1.10) and (1.12) we find the familiar scaling laws for the ionization field $F = 1/16\ n^{-4}$ for the center Stark state (*k*=0) and $F = 1/9\ n^{-4}$ for the extreme red Stark states ($k \approx -n$).

1.4.2 Stark level maps

To calculate the Stark level structure of rubidium, we follow the lines of Ref. [105] and numerically integrate the radial wavefunction using the known quantum defects of Rb. The single-electron Hamiltonian in an external electric field reads

$$\mathcal{H} = \frac{1}{2}\nabla^2 + V(r) + F \cdot z \tag{1.13}$$

We are interested in the energies of the Stark states as a function of field strength, the so-called Stark map. To calculate the Eigenvalues of (1.13), we represent the Hamiltonian in the basis provided by the Eigenvectors $|nlm\rangle$ of the field-free Hamiltonian (1.9). As the Eigenvalues of the field-free Hamiltonian are known, we only have to evaluate the matrix elements

$$\langle nlm|\ F \cdot z\ |n'l'm'\rangle = F \cdot \langle nlm|\ r\cos\theta\ |n'l'm'\rangle$$

The angular part of the matrix elements has well-known analytic solutions in a spherical basis. Using a Numerov algorithm, we can numerically evaluate the radial matrix elements of the Stark operator $\langle n'l'm'|\ r\ |nlm\rangle$ and diagonalize the resulting matrix.

The resulting energy levels for rubidium are shown in Fig. 1.4. The figure demonstrates several important properties of the Stark states of rubidium: (i) the strong suppression of the *s, p, d, f* states due to their quantum defects, (ii) the lifting of the zero-field degeneracy of the $|n, \ell\rangle, \ell > 3$ states, (iii) avoided crossings of appreciable size. Avoided crossings arise from the fact that a non-hydrogenic core breaks the Coulomb symmetry and couples the Stark levels. The size of an avoided crossing is given by the strength of the coupling. Avoided crossings in a time-dependent electric field are discussed in greater detail in chapter 4.

In this thesis, the Stark states of Rb are used in many respects: in chapter 4, field ionization is used to examine the state distribution of Rb Rydberg atoms using state-selective field ionization (SFI). In chapter 6, the fact that the energy difference of two Stark states depends on the applied field is used to make Rydberg atoms a tunable narrow-band detector for far-infrared radiation.

1.4.3 Rydberg atoms in magnetic fields

Analogous to section 1.4.2 and using the approach of Ref. [104] we can calculate the energies of rubidium Rydberg states in an external magnetic field. The Hamiltonian of an atom in an

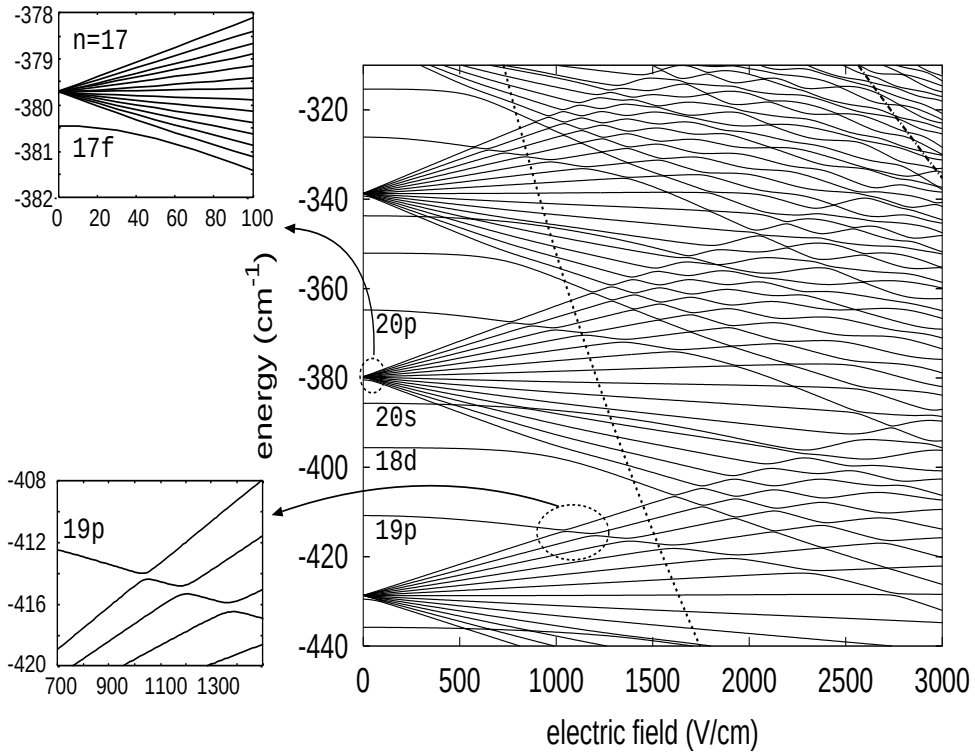

Figure 1.4: Stark map of Rb. The dotted and dash-dotted lines represent the Inglis-Teller and field-ionization limit, respectively. The insets shows the zoom-outs of the circled features. The upper inset shows the f-state mixing with higher-ℓ states, the lower inset shows the avoided crossing of the 19p state with the bluest state of the $n = 16$ manifold.

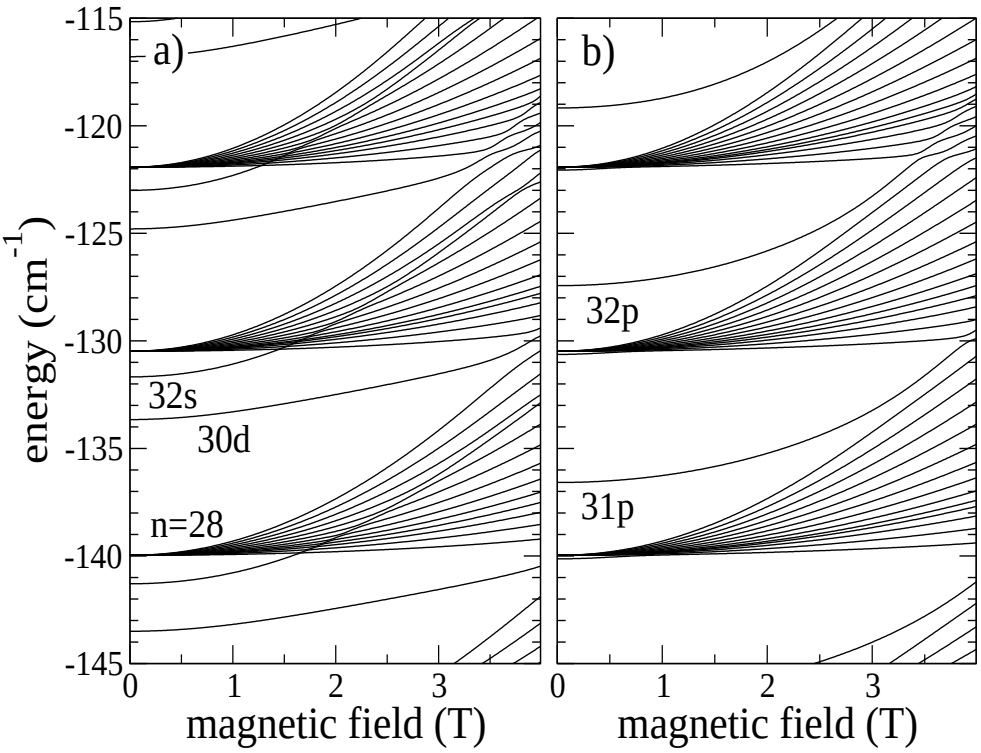

Figure 1.5: Rb Zeeman state energy levels as a function of magnetic field of the (a) even parity and (b) odd parity *m*=0 states around the $n = 29$ manifold.

external magnetic field B in *z*-direction reads

$$\mathcal{H} = \mathcal{H}_0 + A(r)\vec{L}\cdot\vec{S} + \frac{\vec{L}\cdot\vec{B}}{2} + \vec{S}\cdot\vec{B} + \frac{1}{8}(x^2+y^2)B^2 \tag{1.14}$$

where $\mathcal{H}_0$ denotes the zero-field atomic Hamiltonian (1.9). The last term in Eq. (1.14) is proportional to n^4B. For $n^4B \gtrsim 1$ we can ignore the spin $\vec{S}$ as well as the spin-orbit interaction $A(r)\vec{L}\cdot\vec{S}$ to yield

$$\mathcal{H} = \mathcal{H}_0 + \frac{\vec{L}\cdot\vec{B}}{2} + \frac{1}{8}r^2B^2 \tag{1.15}$$

This Hamiltonian couples states of different ℓ, but preserves m as well as the parity, such that only states with $\Delta\ell = 0,\ \pm 2$ and $\Delta m = 0$ are coupled by (1.15). Rydberg states in strong magnetic fields, so-called Zeeman states, display a wide variety of complex features [29]. The energy levels of Rb Rydberg states around *n*=29 as a function of magnetic field are shown in Fig. 1.5. As in the electric field case, large avoided crossings can be seen.

Classical simulation in a magnetic field

In an external magnetic field, the classical equation of motion in atomic units reads

$$\ddot{\vec{r}} = -\frac{\overrightarrow{r}}{r^3} + \dot{\vec{r}}\times\vec{B} \tag{1.16}$$

In a magnetic field, ℓ is not conserved and thus not a good quantum number. In the classical picture, this means that the angular momentum of the orbit changes with time. At *n*=50 and B=1 T the precession time is about 8 ps. If we let the trajectory start at the inner turning point and let the electron propagate in the mixed Coulomb and magnetic field for a longer time, the angular momentum of the orbit evolves.

From quantum mechanical analysis of this system it is known that the lowest and highest states of a Zeeman manifold show spatial localization parallel and perpendicular to the magnetic field, respectively [25]. This property can be included by choosing a localized angular distribution of the trajectories with respect to the *z*-axis.

1.5 Impulse kicks - Interaction of Rydberg atoms with half-cycle pulses

In the chapters 5 and 6 of this thesis, a very peculiar form of electromagnetic radiation is used, namely ultrashort (~ 0.5 ps) pulses with a spectrum ranging from a few GHz to some THz and an electric field which consists in good approximation out of half an optical cycle. These so-called half-cycle pulses (HCPs) interact with Rydberg states in a different way than “many-cycle” optical pulses. In the impulsive approximation, i. e. when the duration of the HCP is much shorter than the Kepler orbit time of the Rydberg state, HCPs transfer

a momentum kick $\Delta\vec{p} = -\int \vec{E}_{\mathrm{HCP}}\,\mathrm{dt}$ to the Rydberg electron at any point in its orbit, where $\vec{E}_{\mathrm{HCP}}$ is the electric field of the HCP. Optical pulses only interact with the part of the electron wavefunction near the core, as in other parts of the orbit $\Delta\vec{p} = 0$ for a many-cycle pulse. The ability of an HCP to transfer a momentum kick $\Delta\vec{p}$ to a Rydberg electron allows us to extract information about the momentum distribution of the Rydberg wavefunction in the kick direction according to the 'impulsive momentum retrieval' method [44]. The energy transferred to the Rydberg atom can be written as

$$\Delta E = p_z \Delta p + \frac{1}{2}\Delta p^2 \tag{1.17}$$

where p_z is the momentum component of the initial state in HCP direction. To produce an electron with zero kinetic energy, the energy change has to equal the binding energy $E_{\mathrm{B}} = -1/(2n^{*2})$, so all electrons with initial momenta $p_z \geq (1/n^{*2} - \Delta p^2)/(2\Delta p)$ will be ionized. Therefore the ionization probability, which can be measured experimentally, is the integral of the probability distribution of the momentum p_z along the HCP axis. The experimental ionization probability of Rb 50d state as a function of HCP field strength is shown along with the result of a classical calculation in Fig. 1.7.

To calculate the ionization probability of a Rydberg atom subjected to an ultrashort half-cycle pulse, we integrate the three dimensional classical equations of motion of an electron in a Coulomb and time-varying electric field using a 4th-order Runge-Kutta algorithm. This method has been shown to agree well with fully quantum mechanical calculations and with experimental data on HCP ionization of Rydberg states [13, 71, 72].

The classical equation of motion of an electron in a Coulomb field subjected to a HCP $\vec{E}_{\mathrm{HCP}}(t)$ arriving at t_{HCP} in atomic units reads:

$$\ddot{\vec{r}} = \frac{\overrightarrow{r}}{r^3} + \overrightarrow{E}_{\mathrm{HCP}}(t - t_{\mathrm{HCP}}) \;, \quad \vec{E}_{\mathrm{HCP}}(t) = \vec{E}_0 \cdot e^{-\frac{4\ln 2 \cdot t^2}{\tau^2}} \tag{1.18}$$

The trajectory starts at $\vec{r}_0$ at the inner turning point with velocity $\vec{v}_0$. Integration delivers $\overrightarrow{r}(t)$ and $\overrightarrow{v}(t)$, which then are used to determine the final energy of the electron. A positive final energy means the atom was ionized in the process. As can be seen from Eq. (1.17) the energy change ΔE can be positive, leaving the atom in a higher lying state or ionizing it, or negative, depending on the sign of $\vec{p} \cdot \Delta\vec{p}$. To obtain the ionization probability of a stationary state we calculate the trajectories for random times t_{HCP} in the range from zero to the Kepler orbit time of the electron $T_K = 2\pi n^3$. As the speed of the electron near the core is much higher than at the outer turning point, the probability to find it near the core is small. A flat random distribution of t_{HCP} provides the correct weighting of the contributions of the different parts of the orbit.

Figure 1.6 shows orbits of a 40d states subjected to half-cycle pulses polarized in *x*-direction with amplitudes of (a) 500 V/cm and (b) 2100 V/cm. The HCPs arrive at different points of time after the electron starts its trajectory at the inner turning point at $t = 0$. At $t = 0.02\,T_K$ (dash-dotted line), the Rydberg electron is moving away from the core and its velocity is parallel to the HCP. $\vec{p} \cdot \Delta\vec{p}$ in Eq. (1.17) is positive and the electron gains energy,

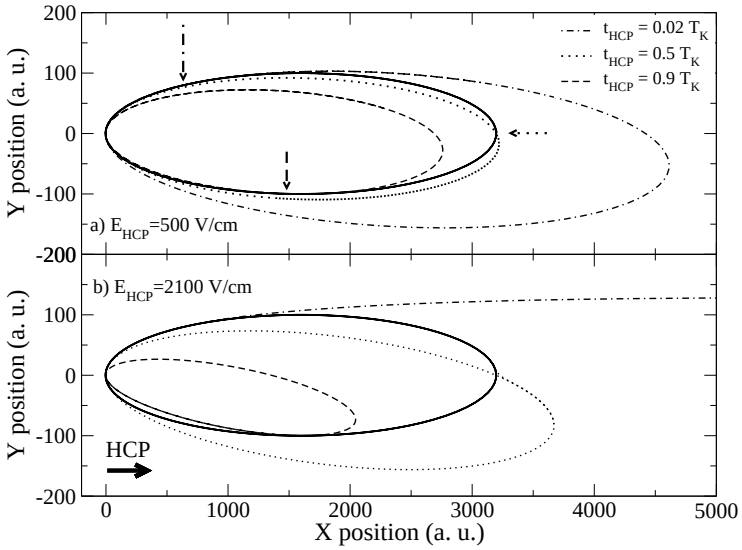

Figure 1.6: Orbits of a 40d state subjected to half cycle pulses with field strengths of (a) 500 V/cm and (b) 2100 V/cm. The electron starts at the inner turning point of the ellipse and travels clockwise. The HCP momentum kick is in *x*-direction. The HCPs arrive after 2% (dash-dotted), 50% (dotted) and 90% (dashed) of the Kepler orbit time. The respective points in the orbit are marked by arrows. The solid line shows the unperturbed 40d orbit.

ending up in a higher orbit. In the case of the stronger kick, the electron gains enough energy to ionize (Fig. 1.6b, dot-dashed line). At $t = 0.5\,T_K$ (dotted line) the electron has reached its outer turning point, where the velocity is very low and the velocity component in the kick direction is zero. The energy change stems purely from the $\frac{1}{2}\Delta p^2$ term. Then the electron turns around, and at $t = 0.9\;T_K$ (dashed line), it is moving antiparallel to the kick. At this point, $\vec{p} \cdot \Delta\vec{p}$ is negative and the electron loses energy, ending up in a more deeply bound state. It takes rather low kick strengths to ionize electrons which move along the HCP, but very high strengths to ionize those which move against the kick. This gives rise to a broad ionization threshold [45].

In reality, the ultrashort half-cycles are followed by a slow low-amplitude negative tail, which has its origin in the fact that a true half-cycle contains zero-frequency fields, which cannot propagate [100]. In the far-field, the integral of the field is zero. By approximating the HCP field shape with a Gaussian, we neglect the influence of the slow negative tail which follows every half-cycle. While these slow negative tails do not qualitatively change the ionization probability of Rydberg states with moderate *n*, they do alter the asymptotic velocity of the ionized electrons dramatically [96].

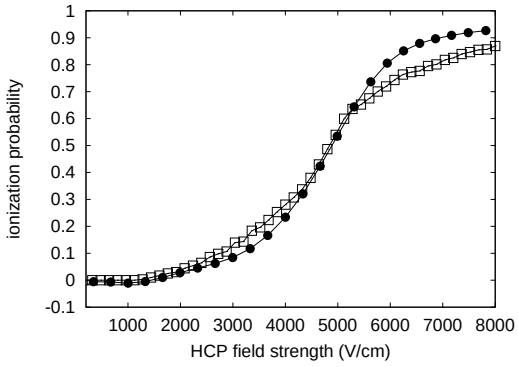

Figure 1.7: Ionization probability vs. HCP amplitude for a 50d state. Experimental data (circles) and semi-classical simulation (squares)

Our calibration of the electric field strength of the HCP as shown in Fig. 1.7 relies on the symmetry of the momentum distribution, i. e. on the fact that as many electrons at a given point of time move in the HCP direction as move against it. Therefore, if 50% of the available Rydberg atoms are ionized by a HCP with peak field strength $E_{50\%}$, electrons with zero momentum in the HCP direction can just ionize with zero kinetic energy. Assuming a Gaussian pulse shape with FWHM τ_{HCP}, Eq. (1.17) gives $\Delta E = \frac{1}{2}\Delta p^2 = E_{50\%}^2 \cdot \tau_{\mathrm{HCP}}^2 \cdot \pi/(4\ln 2) = 1/2n^{*2}$. This calibration is good for states with a Kepler orbit time $2\pi n^3$ which is long compared to the HCP width. For lower *n* states $E_{50\%}$ shows a different scaling law [45, 71]. For very high *n* states (n$\gg 80$), the effect of the slow negative tail of HCPs, which leads to ionization suppression, has to be taken into account [93].

1.6 Example: HCP ionization of Zeeman states

1.6.1 Introduction

In this section we present an experiment on the half-cycle pulse ionization of diamagnetic Rydberg states in a 1 T magnetic field. The highest and lowest diamagnetic Rydberg states of one manifold are known to be localized in space [25]. It has been predicted that half-cycle pulse ionization of these state can be used as a tool to probe localization in Rydberg states of H and Na below the *n*-mixing regime [70]. In this section, we present experiments on a more complex system, namely diamagnetic Rydberg states of rubidium in the *n*-mixing regime. We give an example for the semiclassical simulation described in section 1.5 as well as for some experimental techniques used in the experiments in this thesis.

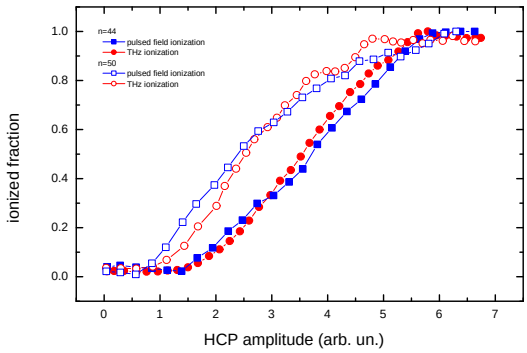

Figure 1.8: Efficiency of HCP ionization in a 1 T field for n=44 (solid symbols) and n=50 (hollow symbols) states as a function of the bias voltage on the THz emitter. The results of two different measurement methods are shown: pulsed field ionization (PFI) of the remaining bound state population (squares) and measurement of the electrons from the HCP ionization (circles). The excitation laser polarization is perpendicular to the magnetic field.

1.6.2 Experimental setup

The experiments were conducted in a magnetic bottle spectrometer capable of producing magnetic fields of 0.99 T [50]. Rb atoms from a thermal beam produced in an oven heated to 360 K are excited to a Rydberg state between n=44 and n=52 with a Nd:YAG-laser pumped nanosecond dye laser in a two photon process. The dye laser beam ($\Delta\lambda = 0.13\,\mathrm{cm}^{-1}$, pulse energy $\approx 300\,\mu$J) is loosely focused into the atom beam between the poles of the electromagnet in the spectrometer. The interaction region is framed by a set of condenser plates spaced by 2 mm. These field plates either generate a small static field (well below the ℓ-mixing regime of n=40) to push electrons ionized by the HCP, or after the THz interaction, a pulsed voltage up to 1 kV is applied to field ionize the remaining Rydberg atoms. In both cases, the electrons are pushed through a hole in one of the poles of the electromagnet into a 50 cm flight tube with a small guiding magnetic field, after which they hit a microchannel plate detector (MCP).

The HCPs are produced using a large-aperture GaAs antenna [101]. A 1 cm piece of semi-insulating GaAs is biased to a voltage of up to 6 kV. Illumination of the GaAs with photons of an energy above the bandgap lifts electrons from the valence band to the conduction band. The carriers are accelerated by the bias field and radiate a short electromagnetic pulse. If the photocarriers are generated on a 100 fs timescale, the radiated pulse contains frequencies up to some THz and has the temporal shape of a half cycle in the near field. We used a

regeneratively amplified Ti:Sapphire laser system which delivers pulses of ca. 70 fs duration at 800 nm with a repetition rate of 1 kHz. To increase the breakdown voltage of the GaAs, we applied a pulsed high voltage. The voltage pulser consists of a car ignition coil with an appropriate circuit which can be triggered by a TTL signal. It delivers voltage pulses of up to 20 kV and can be operated at a repetition rate of 1 kHz.

About 200 ns after the Rydberg excitation by the dye laser pulse, the HCP hits the Rydberg atom cloud and ionizes some of the Rydberg atoms. The HCPs are polarized parallel to the magnetic field. Then either the ionized electrons are pushed towards the MCP by a small static electric field, or the remaining Rydberg atoms are pulsed field ionized by a 5 kV/cm field pulse after a delay of ca. 1 μs and pushed towards the MCP by the ionizing field pulse. The signal is recorded by a digital oscilloscope and the traces are then integrated. In this way, the ionization yield and the remaining bound state fraction can both be measured. The former measurement delivers a better signal-to-noise ratio at low HCP field strength, whereas the latter has the advantage that the ionized fraction is directly observed. Fig. 1.8 illustrates the results of both methods. The ionization probability of *n*=44 and *n*=50 Rydberg states in a 1 T field is plotted against the bias voltage on the THz emitter, which is proportional to the HCP amplitude.

The process of generating HCPs with biased large-aperture semiconductor antennas produces a lot of electromagnetic noise, which is picked up by signal cables etc. in spite of shielding. We used an active baseline subtraction technique to remove as many of the effects of HCP noise in our detected signal as possible. An approach which attacks this problem closer to the source is to put a RC circuit as a local power supply parallel with the emitter [95]. To obtain curves as shown in Fig. 1.8, the pulsed bias voltage across the HCP emitter was increased by a computer-controlled power supply. The voltage across the emitter, which is proportional to the HCP amplitude, was recorded at every data point with a high-voltage oscilloscope probe.

1.6.3 Results on diamagnetic Zeeman states

Figure 1.9a shows the measured ionization probability plotted against the HCP field strength for a $n = 50$ Rydberg state excited with 594.294 nm laser light field free (circles) and in a 0.99 T field with the dye laser polarization parallel (squares) and perpendicular (triangles) to the magnetic field. The curve obtained in a magnetic field is less steep, indicating a broader momentum distribution. This is to be expected from all Zeeman states but the highest, which are localized perpendicular to the magnetic field and thus have a very small momentum component along the field [70]. The lowest Zeeman states are spatially localized along the magnetic field and the intermediate states are not localized. The Laser polarization parallel to the magnetic field excites *m*=0 and the perpendicular polarization can excite *m*=0,-2,2 states. The difference between the curves is very small, although the curve for parallel excitation, i. e. *m*=0 states (squares), is slightly broader. The HCP amplitude needed to ionize 50% of the Rydberg population is not changed by the magnetic field.

Fig. 1.9b shows the calculated ionization probability plotted against HCP field strength for

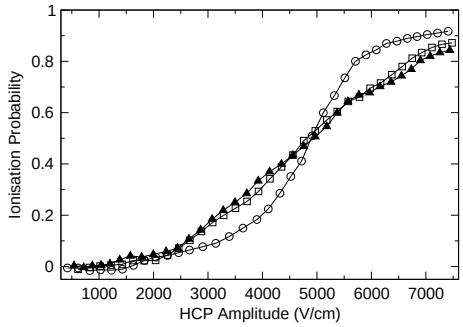

(a) Measured ionization probabilities for a field-free 50d state (circles) and a n=50 Zeeman state in a 0.99 T magnetic field prepared with dye laser polarization parallel (triangles) and perpendicular (squares) to the field.

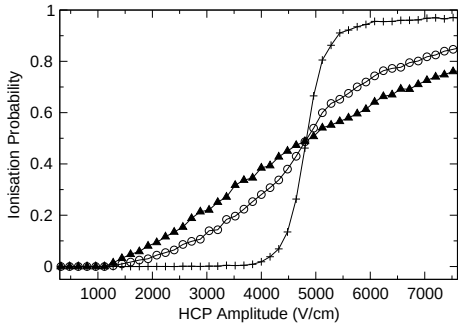

(b) Calculated ionization probabilities for a field-free 50d state (circles) and n=50 Zeeman states in a 1T magnetic field localized perpendicular (crosses) and parallel (triangles) to the field.

Figure 1.9: Measured and calculated ionization probabilities for a field-free 50d state and a n=50 Zeeman state in a 0.99 T magnetic field.

a field free n=50 state (squares) and n=50 states in a 1 T field both localized parallel (triangles) and perpendicular (crosses) to the magnetic field. The Zeeman states localized perpendicular to the field have a very small momentum component in z-direction and therefore a very small spread of momentum in this direction, giving rise to a steep ionization curve (crosses in Fig. 1.9b). States localized along the field and unlocalized states have a broad distribution of momentum in z-direction and therefore display a broad ionization threshold (triangles).

The experimental curve in a 1 T field (triangles in Fig. 1.9a) shows considerable broadening compared to the field-free n=50 state (circles), indicating a broader momentum distribution in the initial state. The calculated ionization curve for a Zeeman state localized along the HCP direction (triangles in Fig. 1.9b) shows the same broadening which is in qualitative agreement with Ref. [70].

Chapter 2

Carrier-phase dependence in the ionization of Rydberg atoms by short radiofrequency pulses

In this chapter we suggest the ionization of Rydberg atoms by radiofrequency pulses as a model system for the ionization process leading to high order harmonic generation. We report time-resolved electron emission in experiments on ionization of rubidium Rydberg atoms (n=90) by few-cycle RF (1-10 MHz) pulses. The electron emission occurs in multiple bursts and strongly depends on the carrier-envelope phase as well as the duration and amplitude of the RF pulses. Due to depletion the emission does not necessarily peak at the highest RF field. A mechanism is identified that spreads the pulsed emission over many RF cycles. Similarities with high order harmonic generation are discussed.

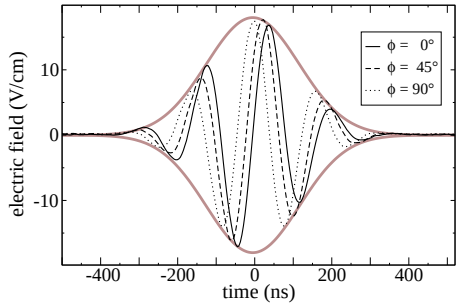

Figure 2.1: Measured radiofrequency pulse shapes with a Gaussian envelope (thick grey lines) and carrier-envelope phases of $\phi = 0$ (dotted line), $\phi = \frac{\pi}{4}$ $(45°$, dashed line) and $\phi = \frac{\pi}{2}$ $(90°$, solid line).

2.1 Introduction

Ionization of atoms by electromagnetic radiation is known to depend strongly on the amplitude and frequency of the driving field. In most cases the role of the phase of the carrier frequency is considered to be irrelevant. Recent calculations [17, 20, 58, 83] and experiments [5, 66] show that for ionization by short pulses containing only a few field cycles, the carrier phase does play an important role. Figure 2.1 shows a field F(t) given by

$$F(t) = E(t) \cdot \sin(\omega t + \phi)$$

with a Gaussian envelope $E(t)$ containing only two cycles at FWHM. As can be seen in the figure, a phase shift $\Delta\phi$ of $\frac{\pi}{2}$ changes the peak value of the central oscillation near the envelope maximum considerably. The peak field is reached twice for $\phi = 0$, but only once for $\phi = \frac{\pi}{2}$. Hence for (nonlinear) processes in which the yield depends strongly on the peak value of the field, the carrier phase of the short pulse can be more important than the frequency. One such process is the emission of high-order harmonics by noble gas atoms upon exposure to intense short optical pulses [52, 78, 103]. In this chapter we describe experiments on a strongly related carrier phase-dependent process: ionization of highly excited Rydberg atoms by a short radio-frequency (RF) pulse. In the experiments we monitored the electron emission with sub-cycle time resolution and found that the emission pattern and total yield strongly depend on the carrier phase of the driving field and that a mechanism exists to spread the emission of electrons in bursts over many RF cycles (see e.g. figure 2.3b).

The similarities between high-order harmonic generation (HHG) in ground-state atoms and ionization of Rydberg atoms by RF pulses are given in table 2.1 and easily explained by a semi-classical description of both processes which assumes an electron orbiting around a point-charge core in an external field. Note that although the characteristic time- and length scales of ground-state and Rydberg atoms are very different, the number of electron

	RF (n=90)	HHG (n=1)
driving frequency (Hz)	10^7	$4 \cdot 10^{14}$
binding energy (Hz)	$4 \cdot 10^{11}$	$3 \cdot 10^{15}$
orbit time $T = 1.5 \cdot 10^{-16} n^3$[s]	10^{-10}	10^{-16}
peak field strength (V/cm)	10	10^8

Table 2.1: Comparison of typical quantities for RF ionization of a n=90 Rydberg state and high harmonic generation by exposing ground-state atoms to 10^{14} W/cm^{-2} of 800 nm radiation.

roundtrips per cycle of the field is much bigger than one in both cases, hence the electron samples the slowly varying potential in many orbits. The frequency of the field divided by the binding energy is much smaller than one in both cases, such that many photons are involved in either case.

The classical HHG model introduced by Corkum in 1993 [18] starts by ionization of the atom by a strong optical laser field. The ionization is considered to take place near the maxima of the optical field cycles by tunneling ionization. The quasi-free electron wave packets are pushed back to the ionic core when the optical field changes sign after about 10^{-15}s. If emitted at the proper phase, the electron revisits the ionic core with a considerable energy gained from the optical field. Then the electron may recombine to the ground state and this energy is released as a VUV[1] or even XUV[2] photon. Such recombination events take place well within an optical cycle of the driving pulse: the XUV emission occurs on an attosecond timescale. This XUV emission process can take place during every half cycle of the optical pulse. The total emission pattern therefore consists of a train of attosecond XUV bursts, rather than a single attosecond pulse [4, 65, 76], unless the driving pulse reaches the few-cycle regime [5]. The tunneling ionization rate strongly depends on the maximum field strength during the cycle, and for few-cycle pulses the electron ejection rate and hence the XUV emission yield are believed to depend on the carrier phase of the optical pulses[20, 83]. Electrons which are ionized at 17° phase delay after the field maximum have the highest recollision energy and produce the highest photon energies in HHG [18].

Similarly, the Rydberg electron in a slowly varying RF field can escape near the peak of the field by tunneling or classical escape over the saddle point in the Coulomb+RF field potential. The emission rate again depends strongly on the field value. For few-cycle RF pulses a carrier phase dependence can be expected on the electron ejection similar to the electron ejection in the ionization process leading to HHG. It should be noted, though, that the low frequencies and the associated long excursions of the ionized electron in the RF field, make the actual recollision and emission of harmonics very unlikely in RF ionization. In HHG, the actual electron emission has never been observed with a sub-cycle resolution.

[1] vacuum ultraviolet, the wavelength region from 200 nm to 100 nm.
[2] extreme ultraviolet, the wavelength region from 100 nm to 10 nm.

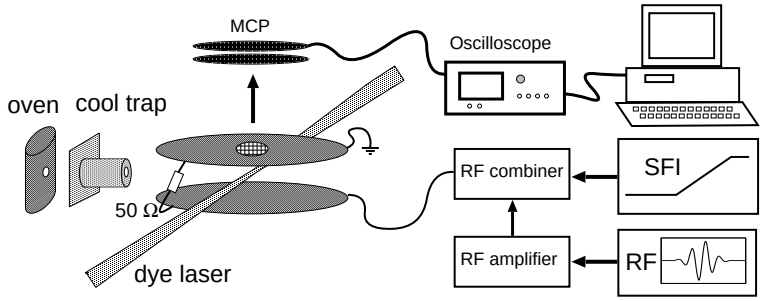

Figure 2.2: Sketch of the experimental setup.

Such observations are frustrated by the high frequency of optical pulses. This constraint is relaxed by about eight orders of magnitude in the case of RF ionization of Rydberg atoms [55, 75], the subject of the experiments described in this chapter.

2.2 Experiment

The experimental setup is depicted in Fig. 2.2. The experiments are performed in a vacuum chamber (10^{-7} mbar). An atomic Rb beam from a resistively heated oven crosses a nanosecond dye laser beam. The laser excites atoms in a two-photon process (λ= 593.72 nm, $\Delta\lambda$ = 0.005 nm) to a high Rydberg state, typically n= 90d. Two capacitor plates, on which the RF field is applied, surround the interaction region. Subsequent to laser excitation the atoms are exposed to the few cycle RF pulse. The RF pulses are synthesized in a programmable pulse generator (Agilent 33250A, frequency range 0-25 MHz), amplified by a RF amplifier and using a transmission line configuration sent to the capacitor plates yielding field strengths up to 50 V/cm. Electrons released by the ionization process are accelerated by the RF field towards the detector. Electrons released at negative half cycles of the RF pulses are pushed towards the detector and recorded with a fast digital oscilloscope, while electrons released at positive cycles are pulled away from the detector. A complete picture of the ionization is obtained by adding two time traces with opposite field polarities. For traces like the ones shown in Fig. 2.3b, we typically averaged the oscilloscope traces over 100 laser shots. The MCP detector has a time resolution of 3 ns, which is much faster than the RF cycle period (100 ns at 10 MHz). The flight time from the interaction region to the detector is about 50 ns, and corrected for by time shifting the electron emission traces. Flight-time dispersion due to different accelerating fields and different starting positions of the electrons is about 15 ns, determining the time resolution of the experiment. Bound Rydberg state population not ionized by the RF pulse is probed afterwards by means of state-selective field ionization. To that end, the field on one of the capacitors plates is ramped in 3.5 μs to 22 V/cm. In the time between

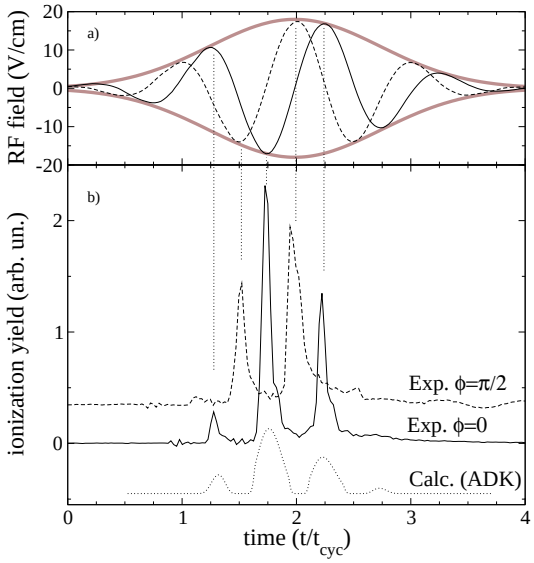

Figure 2.3: a) RF pulses with 6.25 MHz carrier frequency and carrier-envelope phases of 0 (solid) and $\frac{\pi}{2}$ (dashed) as a function of time in units of the cycle time t_{cyc}=160 ns. b) Solid and dashed lines: Experimental ionization yield of a Rb 90d state exposed to the RF pulses shown in a). Dotted line: Ionization yield of ground-state hydrogen subjected to a 10^{15} W/cm^2 optical pulse with a shape as the $\phi = 0$ pulseform shown in a) calculated with an extended ADK formula. For 800 nm, $t_{cyc} = 2.7$ fs.

the laser excitation and the onset of the RF pulse (typically 300 ns), some *m*-mixing of the initially excited *m*=0 state by stray electric and magnetic fields can occur.

2.3 Carrier-phase dependence

Figure 2.3b shows the measured time-resolved electron emission of Rb *n*=90d states exposed to a 6.25 MHz pulse of 1 μs duration (about 2 cycles at FWHM). The emission is compared for two different carrier phases (solid line: $\phi = 0$, dashed line: $\phi = \frac{\pi}{2}$) of the RF field. The integrated power of the pulses is equal within 3%. In both cases the initial Rydberg population is depleted at the end of the pulses. For comparison, the dotted line shows the calculated ionization yield of atomic hydrogen subjected to a 10^{15} W/cm^2 optical pulse with the same field as the $\phi = 0\,^\circ$ trace (solid line) in Fig. 2.3a as obtained from an ADK formula amended by an empirical expression to include barrier-suppression ionization [7]. The following conclusions can be drawn from the observations displayed in figure 2.3. First, the electron emission peaks

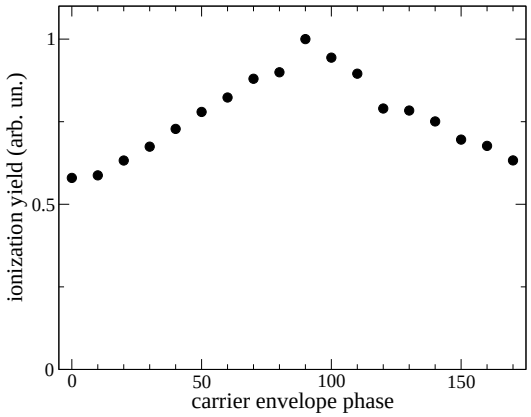

Figure 2.4: Total ionization yield as a function of carrier-envelope phase for a 90d state subjected to a RF pulse with 6 MHz carrier frequency and an envelope amplitude of 14.6 V/cm. The initial 90d state is not depleted after the pulse with a duration of 2 cycles at FWHM.

indeed near the peak of the field. Second, the Rydberg atoms are not depleted in the first half cycle above a certain threshold value, third the emission pattern changes dramatically upon changing the carrier phase of the pulse, as has often been suggested.

It has been predicted that the total ionization yield of ground-state atoms subjected to few-cycle laser pulses depends on the carrier-envelope phase [17]. In Fig. 2.4 we address this question in the radiofrequency domain. The figure shows the integrated ionization yield of a Rb 90d state subjected to a 6 MHz RF pulse with an envelope amplitude of 14.6 V/cm as a function of carrier-envelope phase. The pulse energy in this scan rises about 11% from 0° to 90° carrier phase. The ionization yield increases almost a factor of two if the carrier phase is near $90°$and the cycle amplitude is at the peak of the envelope.

2.4 Details of the ionization process

In figure 2.5 we address why the electron emission is not depleted after the first cycle. Figure 2.5a shows the state-selective field ionization trace of the initial 90d state, i. e. the time-dependent electron emission upon application of a slowly ramped electric field ($\frac{dF}{dt} \approx 6\,\frac{V}{cm\cdot\mu s}$). In an electric field, the degenerate high-ℓ states split up in Stark states. The trace shows two features which result from different pathways while traversing the many crossings of Stark states in the time-dependent field from zero field to the ionization limit. The first, narrow peak comes from pathways which are mostly adiabatic, while the second, broad feature is attributed to mixed adiabatic/diabatic ionization and characteristic for field ioniza-

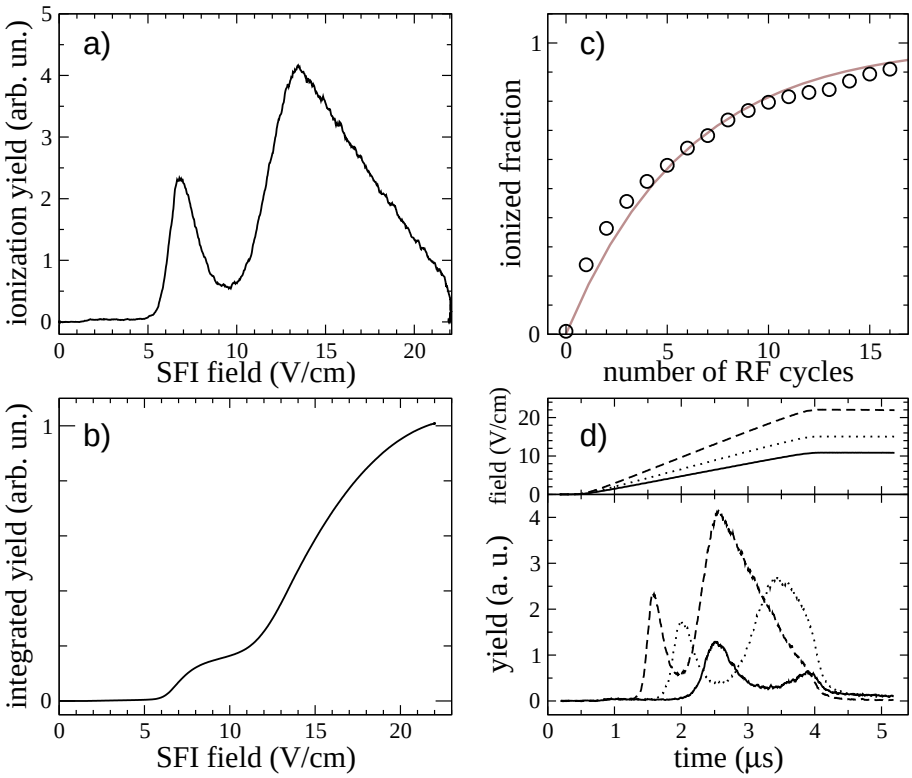

Figure 2.5: a) Field ionization yield of the Rb 90d state by a slowly ramped ($22\,\mathrm{Vcm}^{-1}/3.5\ \mu s$) electric field. b) Integral of a). c) Ionized fraction of the Rydberg population as a function of the number of cycles in a 10 MHz, 13.5 V/cm pulse with a rectangular envelope. The line represents an exponential fit to the data. Each subsequent cycle ionizes ≈20% of the remaining Rydberg population. d) Upper panel: field ramps applied to ionize the 90d state. Lower panel: Time dependence of the electron emission for the field ramps shown in the upper panel.

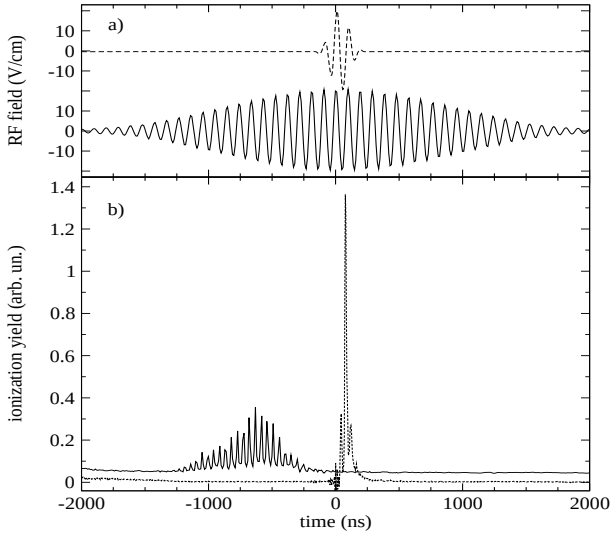

Figure 2.6: a) 10 MHz RF pulses with equal amplitudes of 21.5 V/cm and durations of 95 ns(dashed) resp. $1.2\,\mu$s (solid). b) Electron emission of a 90d state subjected to the RF pulses in a). The traces are set off vertically for clarity.

tion of high angular momentum states (the electric field mixes the angular momenta)[29]. Integration of the total yield gives the ionized fraction at a particular peak-field strength as shown in figure 2.5b. The ionization yield is clearly not a step as a function of the peak field amplitude. This indicates that if in an RF experiment the peak amplitude of a cycle is somewhere on the rising edge of the curve in figure 2.5b, the Rydberg atom population is only partly ionized during that cycle. During the cycle the field lowers again and changes sign and the angular momentum of the remaining bound state fraction of the wavefunction will remix. Such remixing is a non-hydrogenic core effect of the Rb Stark states. At the peak amplitude of the subsequent half cycle again a fraction will be ionized. As a result it takes a few cycles to ionize the Rydberg atom population completely. This is explicitly demonstrated in figure 2.5c, which shows the ionization yield as a function of the number of cycles in a rectangular pulse envelope. This observed behavior at RF frequencies is very similar to the ionization predicted by models used to describe the HHG process at optical frequencies. Fig. 2.5d shows the field ionization process in greater detail. The lower panel shows the time-dependent emission upon application of electric field ramps which rise in $3.5\,\mu$s to 22 V/cm (dashed line), 15 V/cm (dotted line) and 11 V/cm (solid line). It can clearly be seen that once the maximum field value is reached, the ionization rate drops sharply, even if not all the Rydberg population is ionized. Without remixing by the RF field, the remaining population is stable.

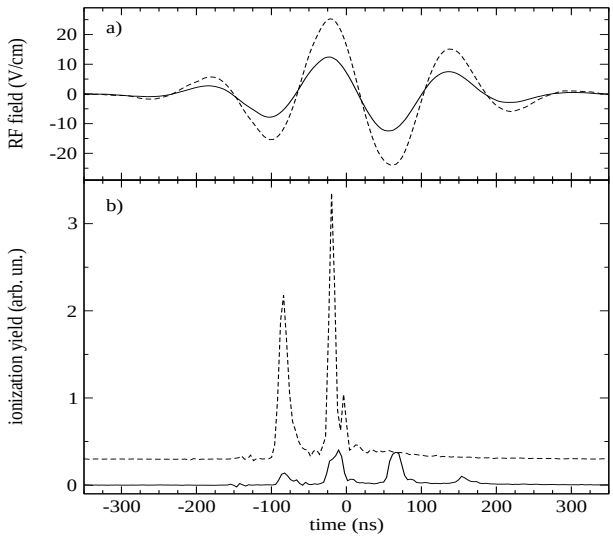

Figure 2.7: a) RF traces with amplitudes 25 V/cm (dashed) and 12.5 V/cm (solid). b) Electron emission traces for the 90d state ionized by the RF pulses shown in a)

2.5 Dependence on pulse duration and amplitude

In HHG, the highest energy electrons are made when the cycle amplitude is maximal and thus photons with the highest XUV photon energy are produced. The experiments shown in figure 2.6 demonstrate why short pulses are advantageous for the generation of high orders of harmonics [76, 103]. The two electron emission traces in figure 2.6b are recorded with two RF pulses (10 MHz, peak amplitude 21.5 V/cm) which have a factor 12 different pulse duration (95 ns, and 1.2 μs, respectively). For the short pulse the population is not yet depleted when the peak of the pulse is reached and a considerable fraction of the electrons is ejected at the peak of the pulse. For long pulses the population is depleted well before the peak is reached [51].

The route to making a single HHG burst rather than a train of attosecond pulses is believed to be using shorter driving pulses. Figure 2.7 shows the electron emission traces for two RF pulses with identical duration but different amplitude. The ionization shifts towards earlier cycles at the stronger pulse, as expected. For the low RF amplitude (solid line in Fig. 2.7), the electron emission is distributed over four peaks, while for the high amplitude (dashed line), the emission is concentrated in only two peaks. This shows that not only the duration, but also the amplitude determines in how many cycles the electron wavefunction is ejected. Note that although the highest field amplitude is reached twice in the pulse, for the strong pulse only one burst contains electrons ionized (and accelerated) by the highest amplitude.

The harmonic cutoff for a given atomic system and laser frequency is determined by the laser intensity, i. e. the field strength [49]. This implies that the highest order harmonics produced by a pulse which corresponds to the dashed line in Fig. 2.7 are produced by a single half cycle. Optical high-pass filters which pass only the highest harmonics could thus single out an attosecond pulse from a pulse train.

2.6 Conclusions and outlook

Nowadays, optical pulse synthesizing techniques [5, 11, 92] allow for shaping of complex pulse forms. Anticipating on such research in the optical domain we investigate the effects in the RF domain. In figure 2.8 we compare the details of the emission pattern for sinusoidal waves versus triangular waves, with similar pulse envelopes. Both shapes show a peak splitting of the electrons, this is attributed to diabatic and adiabatic pathways of the electron amplitude while traversing the Stark map. The height of the peaks differs for the triangular RF pulse as opposed to the sinusoidal pulse. Detailed understanding of this double-peak phenomenon requires further experiments and theoretical modeling and can contribute to the discussion over the optimal pulse shape for HHG. An interesting question is how different pulse shapes can be employed to optimize a desired ionization behavior.

In conclusion, we observed that the electron emission of Rydberg atoms exposed to few-cycle RF pulses occurs in multiple bursts. The actual pulse parameters (amplitude, frequency *and* phase) determine the number and relative height of the emission peaks as well as the field value at which the maximum emission occurs. The investigated system displays many similarities with the physics underlying high-order harmonic generation and is believed to be an ideal model system. Sophisticated theoretical modeling is needed to understand all of the observed features and their possible implications for HHG.

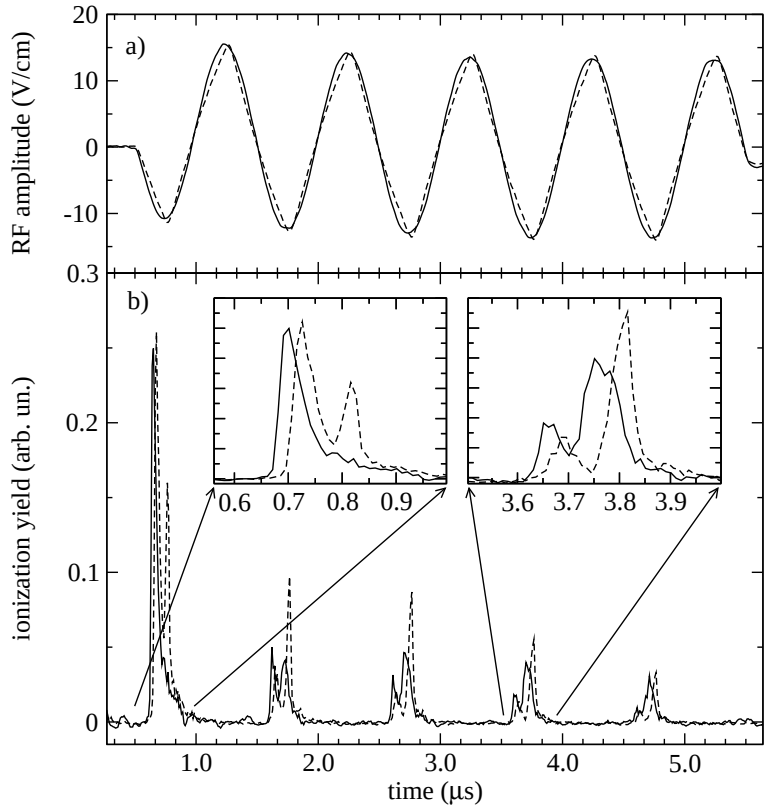

Figure 2.8: a) 1 MHz RF pulseforms with sine (solid) and triangular (dashed) shapes. b) Electron emission traces of a 90d state subjected to the RF pulse forms shown in a). Only the ionization by the negative part of the RF is shown.

Chapter 3

Asymmetry in the ionization of Rydberg atoms by few-cycle pulses

In this chapter we present measurements of the electron ejection direction in the ionization of high (n=90) Rydberg states of rubidium subjected to few-cycle radiofrequency pulses. We find the ejection highly asymmetric in the polarization direction and strongly dependent on the pulse parameters amplitude, duration and carrier-envelope phase. The asymmetry disappears for pulses longer than 4 cycles, comparable to the results for optical pulses reported by Paulus et al. (Nature 414, 182 (2001)). For strong pulses the ejection direction becomes a complex function of the pulse parameters and the asymmetry persists up to 9 cycles.

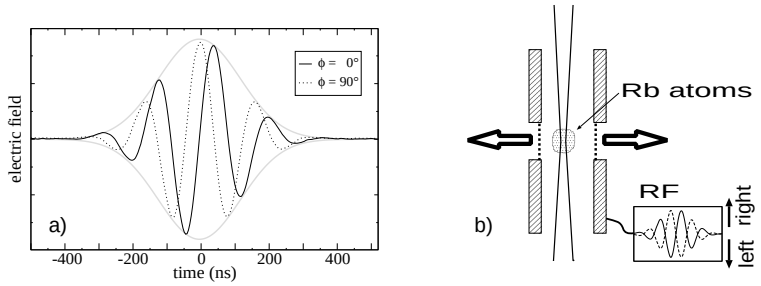

Figure 3.1: (a) Radiofrequency pulses with 6 MHz carrier frequency and carrier-envelope phases of 0 (solid) resp. 90 (dashed) degrees. (b) Sketch of the experimental setup to measure the ionization yield in left/right direction. In the experiment, instead of measuring on the left and right side of the interaction region, the amplitude of the RF is inverted.

3.1 Introduction

Non-linear processes in atomic and molecular physics have intrigued researchers ever since high-intensity laser sources became available. Notable examples are above-threshold ionization (ATI) [1, 19, 28], Coulomb explosion [68] and high-order harmonic generation [52, 78, 103]. By definition, these nonlinear processes depend strongly on the oscillating electric field of the driving laser pulse. For the shortest available pulses ($\tau \approx 5$ fs, λ =800 nm), the pulses contain only a few cycles of the optical field. In this domain, the exact phase between the carrier wave and the envelope becomes important. While the envelope of a short laser pulse can be controlled with high precision nowadays[12, 92], the control of the exact electric field, i. e. the carrier-envelope phase, has proven much more challenging and has been accomplished only very recently [5]. The electric field

$$E(t) = E_0 \cdot e^{-\frac{t^2}{\tau^2}} \cdot \sin(\omega t + \phi)$$

for a few-cycle pulse with Gaussian envelope and carrier-envelope (C-E) phases of $\phi = 0$ and $\phi = 90$ degrees is shown in Fig. 3.1a.

In photoionization, the ionized electrons are almost always emitted uniformly in the direction of the positive and negative optical field and the angular distribution of the photoelectrons is determined by the initial and final (continuum-) states of the atom, i. e the frequency, polarization and intensity of the driving laser field. Angular distributions of photoelectrons in ATI experiments have been reported using ground-state atoms exposed to optical pulses [77] as well as Rydberg atoms exposed to many-cycle microwave pulses [6, 28]. Paulus and coworkers recently demonstrated by measuring a contingency map, that for pulses containing only a few cycles of radiation, the emission direction becomes dependent on the carrier-envelope phase [66]. This dependence was confirmed by Keldish theory [58] and numerical solution of the time-dependent Schrödinger equation for hydrogen in an intense 800 nm field [15].

In multi-photon ionization of ground state atoms, high intensity laser pulses produce fields $\gtrsim 10^8$ V/cm which suppress the binding Coulomb potential enough to allow the atom to ionize by tunneling. In contrast, for highly excited Rydberg atoms the fields needed to ionize are in the order of a few V/cm. The orbit time of the Rydberg electron, on the other hand, is about 6 orders of magnitude longer than that of a ground state atom. The combined dynamics of the atomic system and the time-varying field of a n=90 Rydberg state subjected to a 10 V/cm radiofrequency (RF) pulse and a ground state atom subjected to a 10^8 V/cm optical pulse are therefore comparable. An advantagous aspect of experiments at RF frequencies is the continous control of all pulse parameters. In this chapter, we describe the ionization of Rydberg states by few-cycle radiofrequency pulses and establish the dependence of the emission direction on the amplitude as well as the carrier-envelope phase and the number of cycles in the pulse. We compare our results with optical experiments where such control over the pulse parameters is difficult to achieve.

3.2 Experiment

RF pulses are easily synthesized in arbitrary waveforms. For the experiments presented here, we used an Agilent 33250A arbitrary pulseform generator to produce pulse forms with a Gaussian envelope and carrier frequencies of up to 25 MHz with controllable C-E phases as shown in Fig. 3.1a. The generated pulse forms are then amplified by a RF amplifier to amplitudes of up to 25 V. In the experimental setup (see Fig. 3.1b) we excite Rb atoms from a resistively heated oven to a Rydberg state around n=90 using a 10 Hz narrow-band nanosecond dye laser. The excitation takes place between two capacitor plates spaced by 4.65 mm which are set up in a 50 Ω transmission line configuration for the radiofrequency. The RF pulse is applied to one of the plates 200 ns after excitation. Electrons ionized by the negative part of the RF are pushed through a grid-covered hole in the second plate by the RF field. The electron yield is detected with a microchannel plate detector (MCP) with sub-cycle time resolution. The emission in the other direction is measured by repeating this procedure with the inverted pulse form, such that now electrons ionized by the positive part of the first pulse are detected. In the time from excitation to ionization of the Rydberg atoms, the initially excited 90d state evolves through processes like precession in the earth magnetic field into states with higher angular momenta and magnetic quantum numbers. The resulting mixture of states displays a broad threshold for electric field ionization and ionizes in bursts upon application of a RF field [35].

3.3 Dependence of the ejection direction on the amplitude

In Fig. 3.2 we show the influence of the RF amplitude on the symmetry in the ejection of the ionized electrons. We plot the ionization yield for a 90d Rydberg state subjected to a 300 ns RF pulse with a Gaussian envelope and 6 MHz carrier frequency dependent on the RF

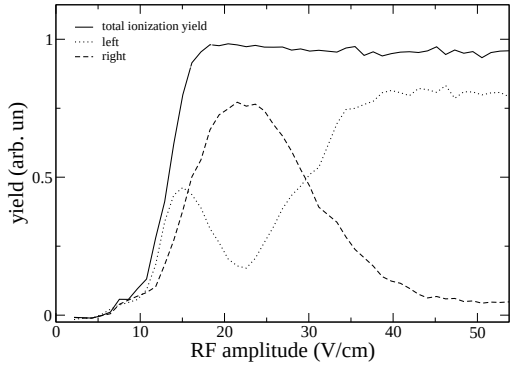

Figure 3.2: Ionization yield ejected to the left (dotted line) and to the right (dashed line) for a 90d initial state subjected to a 6 MHz, 300 ns pulse with a carrier-envelope phase of 45°. The solid line shows the total ionization yield. For low ionized fractions, the angular distribution is uniform. As the ionization becomes non-negligible, the ejection direction gets more and more dependent on the amplitude.

amplitude. The carrier-envelope phase is set to 45°. The dotted and dashed lines represent the electron yield ejected in left resp. right direction, the solid line represents the total ionization yield. The curve can be roughly divided into three sections: for very low amplitudes, the electron flux is spread evenly over both directions. The ionized fraction is negligible, such that each subsequent half-cycle finds the same situation and ionizes a certain fraction. For the 45° pulse shape, two half-cycles contribute to the ejection in each direction and in this situation this results in symmetric ejection. For amplitudes higher than ≈11 V/cm a slight asymmetry can be seen. In this region, more than 10% of the Rydberg population is ionized by the RF pulse, such that the order in which the half-cycles follow upon each other becomes important. Finally, for RF amplitudes exceeding 20 V/cm, the Rydberg population is depleted at the end of the pulse. In this region, a considerable fraction of the population is ionized by a single half cycle and the emission becomes directional. For even higher amplitudes, an earlier half-cycle takes over and the emission direction is reversed.

The complete ionization process for RF amplitudes of zero to 50 V/cm and for carrier-envelope phases of 0 and 90° is shown in Fig. 3.3. We plot the time-resolved ionization traces along the vertical axis, darker colors mean more ionization. Every second peak is ejected to the left respectively to the right. It is clearly to be seen that the ionization shifts to earlier times with increasing RF amplitude as earlier cycles take over the ionization process. It should also be noted that for the 0° (Fig. 3.3a) traces, up to three half-cycles contribute to the ionization process, whereas for the 90° pulses (Fig. 3.3b), one or two half-cycles contribute.

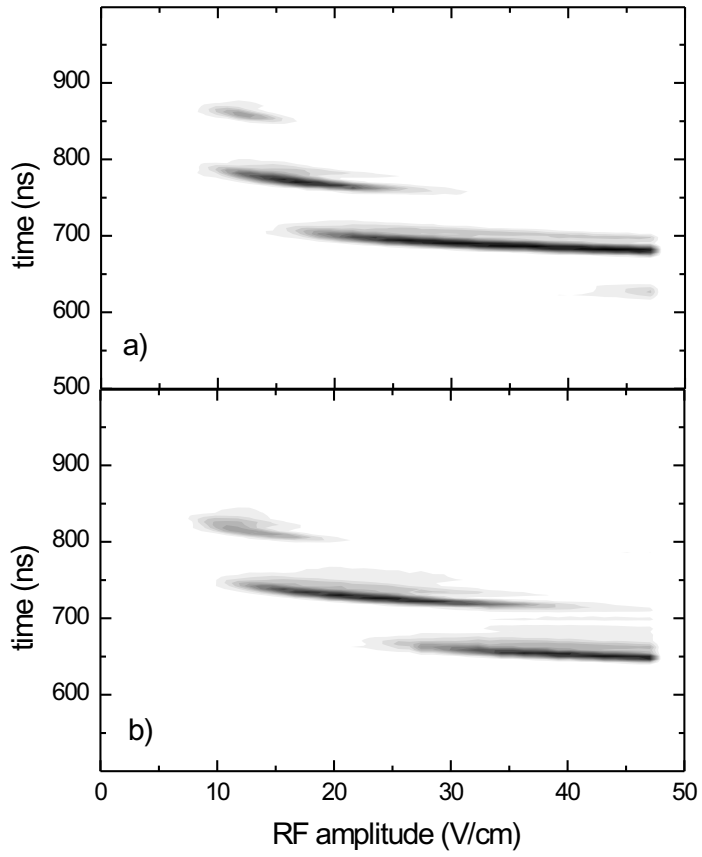

Figure 3.3: Time-resolved ionization emission traces of a Rb 90d state subjected to RF pulses with carrier-envelope phases of a) 0° and b) 90° and amplitudes of zero to 50 V/cm.

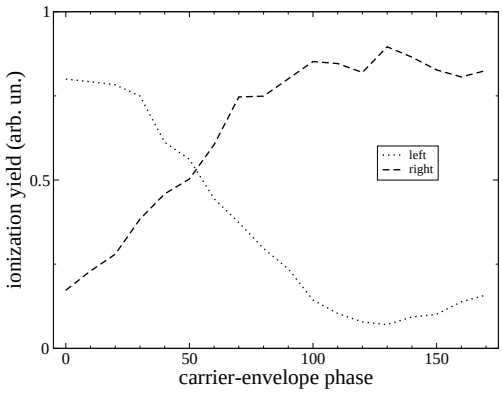

Figure 3.4: Electron yield ejected to the left (dotted line) and the right (dashed line) as a function of the C-E phase for a 90d initial state subjected to a 6 MHz, 300 ns pulse with an amplitude of 30 V/cm.

3.4 Dependence of the asymmetry on the carrier-envelope phase

For a fixed RF amplitude of 30 V/cm we scanned the C-E phase from 0 to 180°. The result is shown in Fig. 3.4. The number of electrons ejected in one direction is clearly very sensitive to the C-E phase under these circumstances and in most cases highly asymmetric. It should be noted that the Rydberg population is depleted after the pulse. Clearly, the ejection direction does not behave as one would expect by looking at the RF shapes shown in Fig. 3.1a, from which one might expect a symmetric emission for a C-E phase of $\phi = 0$ and a directed emission for $\phi = 90°$. Instead, the yield in both directions is equal at $\phi \approx 53°$. To look into this further, we define an asymmetry parameter

$$a = \frac{\mathrm{yield}_{\mathrm{right}} - \mathrm{yield}_{\mathrm{left}}}{\mathrm{yield}_{\mathrm{left}} + \mathrm{yield}_{\mathrm{right}}}$$

which is zero for a symmetric ejection in both directions and ± 1 for fully directional emission to one side. We define "left" as the direction of the negative field.

In Fig. 3.5 we plot the asymmetry parameter depending on the C-E phase for RF amplitudes of 13 V/cm (dashed line), 23 V/cm (dotted line) and 30 V/cm (solid line) and a pulse containing about two cycles at full width half maximum (FHWM). It is apparent that the curves are very different. Comparison with Fig. 3.2 shows that the initial Rydberg population is depleted after the pulse for amplitudes $\gtrsim 18\,\mathrm{V/cm}$. Only for low RF amplitudes (dashed line) the asymmetry behaves as expected from the RF pulse shape, i. e. symmetric ejection for $\phi \approx 0, 180°$, which is a point symmetric shape (compare Fig. 3.1a) and an asymmetric

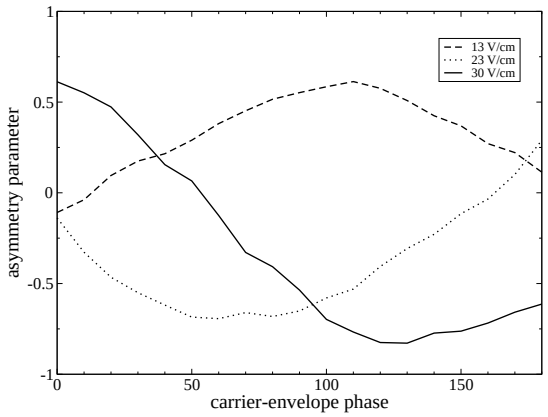

Figure 3.5: Dependence of the ejection direction on the carrier-envelope phase. Shown is the ejection asymmetry parameter for RF amplitudes of 13 V/cm (dashed line), 23 V/cm (dotted line) and 30 V/cm (solid line). A value of zero means symmetric ejection in both directions. The Rydberg population is depleted for amplitudes $\gtrsim 18\,\mathrm{V/cm}$. The 6 MHz pulses are 300 ns long.

emission for $\phi \approx 90°$, for which the highest amplitude is reached only once. The shift of 10° can be attributed to stray electric fields caused e. g. by contact potentials of Rb deposited on the plates and slight asymmetries in the RF pulse shapes. For high RF amplitudes (dotted and solid lines), the ionization process is easily dominated by a few or even a single half-cycle of the RF field. Therefore the ejection becomes highly directional, depending on the exact pulse shape. If we follow the solid line in Fig. 3.5 (highest field), the emission is dominated by a single half-cycle in "left" direction just before the peak of the envelope at $\phi = 0$. With growing C-E phase, this half-cycle ionizes less and less and a second, later half-cycle with opposite polarity begins to contribute until both of them contribute equally to the ionization signal at $\phi \approx 53°$. The influence of the first half-cycle further decreases and a third half-cycle again in "left" direction starts to contribute at $\phi \approx 140°$. For even higher C-E phases, the influence of the third half-cycle grows. This shows that for high amplitudes the exact behavior is complex and depends on the details of the underlying strong-field ionization mechanisms.

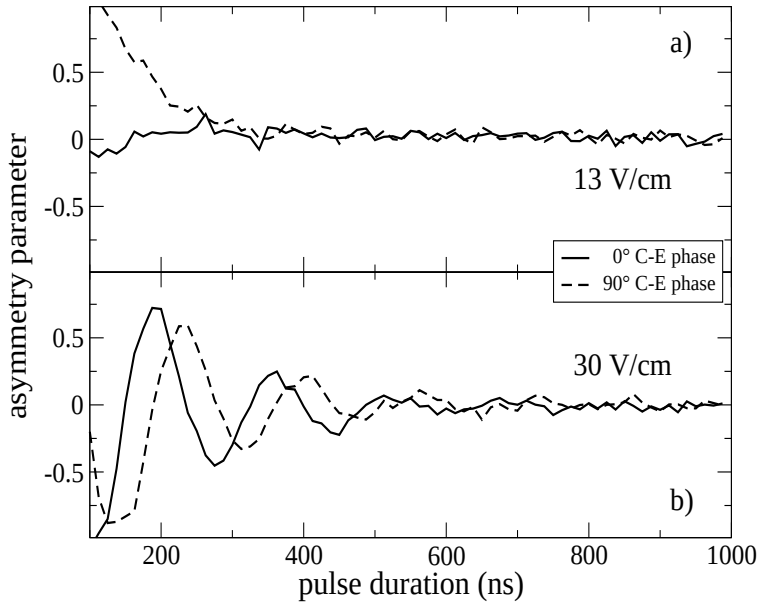

Figure 3.6: Left/right asymmetry dependence on the pulse duration of a pulse with 12.5 MHz carrier frequency, 0°C-E phase (solid line) and 90°C-E phase (dashed line) and amplitudes of a) 13 V/cm and b) 30 V/cm RF amplitude. The ionization process is only directional for few-cycle pulses, for longer pulses the emission becomes symmetric.

3.5 Influence of the pulse duration

For pulses with Gaussian envelopes, directed emission in one direction can occur only with few-cycle pulses. This is explicitly demonstrated in Fig. 3.6, where we show the ionization asymmetry parameter as a function of pulse duration for pulses with 12.5 MHz carrier frequency and a Gaussian envelope of constant amplitude. RF pulse forms with 0° C-E phase (solid lines) and 90° C-E phase (dashed lines). In Fig. 3.6a we show data for a RF amplitude of 13 V/cm which ionizes 30-75% of the initial Rydberg population, depending on pulse length. The emission of the sine pulse ($\phi = 0^\circ$, solid line) is symmetric for all pulse durations. For the cosine pulse ($\phi = 90^\circ$, dashed line) the single half-cycle with maximal field strength defines a preferred ionization direction in the short-pulse (few-cycle) limit. With increasing pulse duration the emission quickly becomes symmetric at a pulse length of ≈ 300 ns ($\approx$4 cycles at FWHM) as multiple half-cycles contribute to the ionization process. This can be compared with measurements in the optical domain where the asymmetry disappeared when they changed the pulse length from 6 fs to 8 fs (≈ 3.5 cycles) [66]. The situation for high

RF amplitudes as shown in Fig. 3.6b is entirely different. Both the 0° and 90° curves show strongly directed electron ejection. The ejection direction oscillates as the pulse duration is increased and the asymmetry disappears for long durations, i. e. many-cycle pulses. For durations longer than $\approx$ 700 ns (9 cycles at full width half maximum) the emission becomes symmetric. Again, for high RF amplitudes the ionization is mostly done by one half-cycle. The effect of increasing the pulse duration while keeping the envelope amplitude constant in this case is to enable an earlier half-cycle to ionize most of the Rydberg population such that the ejection direction reverses. For long pulses, the ionization is spread over many half-cycles on the rising edge of the pulse and the emission becomes symmetric.

Fig. 3.6b also suggest a direction for further experiments in the optical domain. For very strong fields this oscillatory behaviour should be present in the optical case as well. As the pulse energy is not easily increased to arbitrary values, the use of an alkali metal such as rubidium or cesium with a much lower ionization potential than the widely used noble gases could allow for this kind of experiments even at today's pulse energies.

3.6 Conclusions

It has been suggested that the asymmetry in ionization could be used to determine the C-E phase of a few-cycle pulse[66]. The results at RF frequencies shown in Fig. 3.5 do not display an unambiguous relationship between the asymmetry and the phase, indicating that the asymmetry should be measured for at least two intensities in the strong-field regime to deduce the C-E phase from the result.

In conclusion we measured the ejection direction of Rydberg electrons ionized by radiofrequency pulses depending on amplitude, duration and carrier-envelope phase of the pulses. We found that the ejection direction for low RF amplitudes strongly depends on the C-E phase for short pulses. For high amplitudes, the ejection direction is always asymmetric and strongly depends on the exact field for few-cycle pulses. For many-cycle pulses the electron emission becomes symmetric in both cases.

Chapter 4

State-selective field ionization of rubidium

We demonstrate a refinement of the state-selective field ionization technique which is widely used for the state-selective detection of Rydberg states. The selectivity of this technique is improved considerably and extended to ℓ-states in heavy alkalis by employing shaped field ramps. We show the increased selectivity of field ionization by a fast step followed by a slow ramp in rubidium and apply this scheme to an electron scattering experiment, corroborating dipole selection rules in fast electron scattering induced excitation.

4.1 Introduction

Time-resolved measurement of the ionization of Rydberg atoms by slowly ramped electric fields, so-called state-selective field ionization (SFI), has been used for many years to determine the final state distribution in experiments investigating the physics of highly excited states. Of the multitude of experiments using SFI some examples are microwave excitation of Rydberg atoms [90], electron- and ion-collision experiments [27, 80], half-cycle pulse excitation [97], far-infrared spectroscopy [24] and electron-ion recombination [94]. On the theoretical side, the Landau-Zener model of traversing the Stark map from the regime where neighboring *n*-manifolds cross [40] to the ionization limit has led to a complete model for ramped-field ionization [73].

In many of those experiments, sodium has been used as the target atomic system. The reason for this choice is the fact that SFI in sodium offers a much higher selectivity than it does in the heavier alkalis rubidium and cesium, such that not only the principal quantum number *n*, but also the angular momentum ℓ and the even the magnetic quantum numbers *m* could be resolved [31] in certain cases. In the heavier alkalis the resolution is frustrated by spin-orbit effects[32]. Conversely, rubidium offers considerable experimental advantages, such as the low melting point and high vapor pressure and the low ionization potential which makes the Rydberg states of interest accessible using only one dye laser at a convenient wavelength around 595 nm. Rubidium is also commonly used in Bose-Einstein condensation experiments, resulting in a large amount of literature on the trapping and cooling of Rb and on the techniques for stabilizing the required diode lasers [57]. For these reasons, applications of Rydberg atoms such as the recently reported infrared and far-infrared imaging photocathodes [23, 33] are likely to rely on the heavier alkalis. Other reported applications, like atomic streak cameras [89] or an atomic XUV spectrometer[88] make use of a wide range of elements depending on the wavelength they operate at. Although not all of the named devices use SFI directly, for many of them improvements based on SFI are in discussion. Therefore it is desirable to obtain a higher SFI selectivity in elements such as Rb. Shaped SFI ramps have been used to apply SFI to Stark states and states with very high principal quantum number n [21, 81]. In this chapter we report an improvement of the SFI technique based on carefully shaped ramped fields and a fitting procedure using measured SFI spectra of optically accessible states. We use an electron scattering experiment to demonstrate the improved selectivity in Rb.

4.2 State-selective field ionization

An electric field introduces a saddle point to the Coulomb potential at an energy of

$$E_{\mathrm{SP}} = -6.12 \cdot \sqrt{F} \ \left(\mathrm{cm}^{-1}\right) \tag{4.1}$$

where *F* is the electric field given in V/cm. In non-hydrogenic atoms, all states with an energy greater than E_{SP} are coupled to the continuum and in the end ionize. For SFI, an electric field

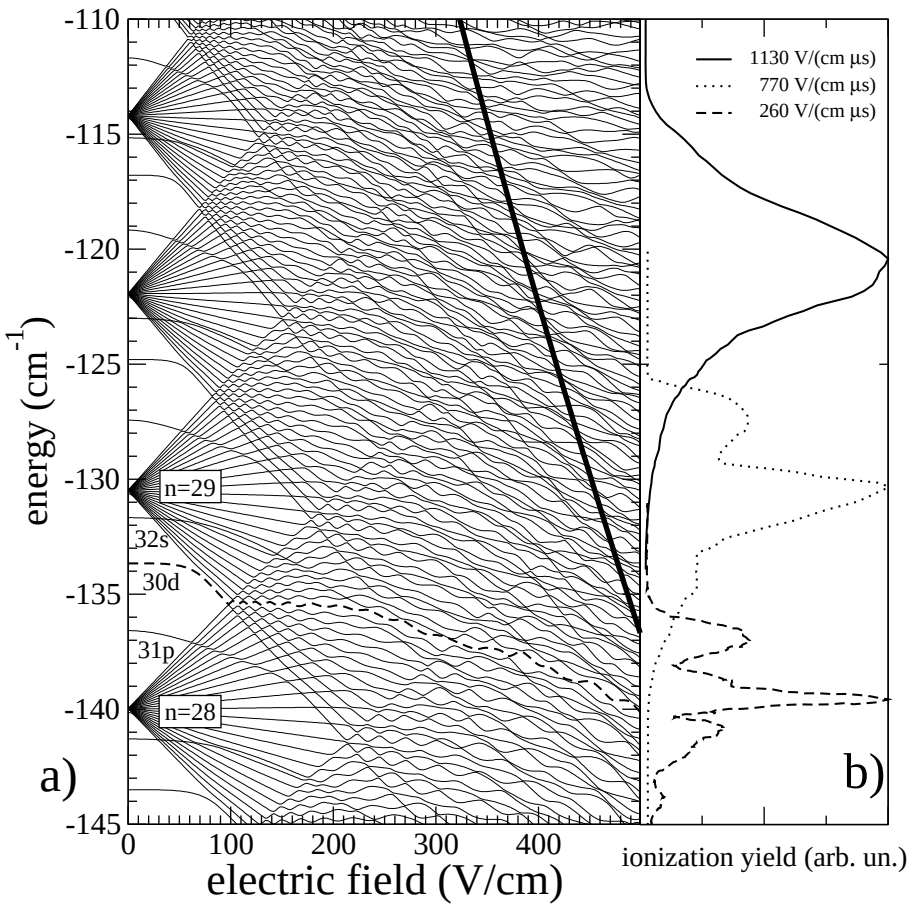

Figure 4.1: a) Energy levels of the Rb m=0 states as a function of the electric field around the n=29 manifold. The dotted line is the adiabatic path of the 30d state. The solid line denotes the ionization threshold. b) SFI traces of an initial 30d state taken with SFI slew rates of solid line: 1130 V/(cm·μs), dotted line: 770 V/(cm·μs) and dashed line: 260 V/(cm·μs). The vertical axis is the saddle point energy in the SFI field (see text).

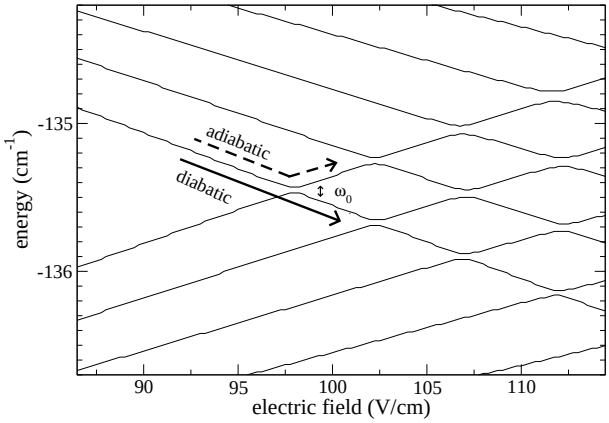

Figure 4.2: Stark map of the crossing of the bluest Stark states of the n=28 manifold with the reddest states of the n=29 manifold from Fig. 4.1 in greater detail. The adiabatic and diabatic pathways are marked by dashed and solid arrows, respectively. The separation of the states at the avoided crossing is ω_0.

is slowly ramped until the populated states are ionized. The time of ionization marks the field at which the states ionize, which is then a measure of the energy of the state before ionization. In Fig. 4.1a we show the rubidium Stark levels of the n=28 to 31 manifolds as a function of the static external electric field. The adiabatic route of the 30d state is denoted by a dashed line. The thick line denotes the saddle point energy as given by Eq. (4.1). The *s*, *p* and *d* states of Rb have large quantum defects and are clearly set off the degenerate manifold of high-ℓ states with the same n^*. It is clear that in traversing the Stark map from zero field to the ionization limit, the Rydberg state encounters many avoided crossings which can be traversed adiabatically or diabatically, depending on the slew rate of the field. In general, at every crossing the population partially follows the diabatic and the adiabatic pathway. In Fig. 4.1b SFI traces are shown which were taken with slew rates of $1130\,\mathrm{V/cm}\cdot\mu$s(solid line), $770\,\mathrm{V/cm}\cdot\mu$s (dotted line) and $260\,\mathrm{V/cm}\cdot\mu$s (dashed line) after excitation of the 30d state in field free conditions. The horizontal axis gives the ionization yield in arbitrary units and the vertical axis is the SFI field converted to the saddle point energy using Eq. (4.1). It is obvious that the SFI traces for different slew rates look very different and depend strongly on the exact pathway the population follows on its way from zero field to the ionization limit. The slowest ramp ($260\,\mathrm{V/cm}\cdot\mu$s) leads to a completely adiabatic traversal of the Stark map. For faster ramps, some of the crossings are traversed diabatically, resulting in a significantly lower ionization field in this case. In all of the cases studied here, the 30d state traverses the first crossing at 70 V/cm in Fig. 4.1a adiabatically.

The region where the rubidium n=28 and n=29 manifolds cross is shown in detail in

Fig. 4.2. In the Landau-Zener approximation, the probability to traverse an isolated avoided crossing diabatically is given by [48]

$$P_{\mathrm{dia}} = \exp\left(-\frac{2\pi|V_{12}|^2}{\hbar \cdot (\mathrm{dW}_{12}/\mathrm{dt})}\right) \tag{4.2}$$

where V_{12} is the coupling matrix element of the interaction that causes the avoided crossing and W_{12} is the energy difference between the two states. The separation of the states at the avoided crossing ω_0 is $2V_{12}$. The time derivative of the energy difference can be rewritten as

$$\frac{\mathrm{d}W_{12}}{\mathrm{dt}} = \dot{F} \cdot \left|\frac{\mathrm{d}E_1}{\mathrm{d}F} - \frac{\mathrm{d}E_2}{\mathrm{d}F}\right| \tag{4.3}$$

with $\dot{F}$ being the slew rate of the field and $\frac{dE}{dF}$ the gradients of the two involved states in the Stark map (see Fig. 4.2). Using the calculated avoided crossings the Landau-Zener probabilities can be estimated. For the slowest ramp in Fig. 4.1, the diabatic probability for the crossing indicated in Fig. 4.2 is on the order of 10^{-9} and the traversal is adiabatic. For the fastest ramp, $P_{\mathrm{dia}} \approx 0.01$ such that this crossing is traversed predominantly adiabatically resulting in an upward-going Stark state. However, later crossings might be traversed diabatically, leading to the behaviour seen in Fig. 4.1. From this example it can be seen that how the wavefunction traverses the Stark map depends both on the initially excited state and the slew rate of the field. In rubidium, however, this does not lead to a selectivity which is high enough to resolve the populations in neighbouring $\ell-$states. In this chapter we make use of the slew-rate dependence of the pathways and use SFI ramps constructed from an initial fast step followed by a slow ramp to obtain SFI traces with increased selectivity.

4.3 Experimental setup

The experimental arrangement for the SFI experiment is straightforward. Rubidium is evaporated in a resistively heated oven at $\approx 70^\circ$ C. The effusive beam is directed between two capacitor plates spaced by 5 mm. The upper plate contains a hole covered by a grid. A dye laser pumped by a Nd:YAG laser ($\approx 800\,\mu$J) is loosely focused between the capacitor plates, exciting the Rb atoms into a Rydberg state. To excite *s*- and *d*-states, a non-resonant 2-photon excitation is used, and for the excitation of *p*-states, the light is doubled in a KDP crystal. The shaped SFI ramp is applied to the lower plate.

The ramp is generated by an Agilent 33250A arbitrary pulseform generator and then amplified by a home-built fast high-voltage amplifier (1 MHz bandwidth, 400 V output). Electrons ionized by the SFI field are pushed towards a microchannel plate detector (MCP). The electron signal and the SFI field are monitored by a digital oscilloscope and stored on a computer. The setup is depicted in Fig. 4.3. To demonstrate the method, we used an electron scattering experiment where we investigate the redistribution of Rydberg population to neighboring states by fast electron collisions. To that end, electrons are extracted from a Philips

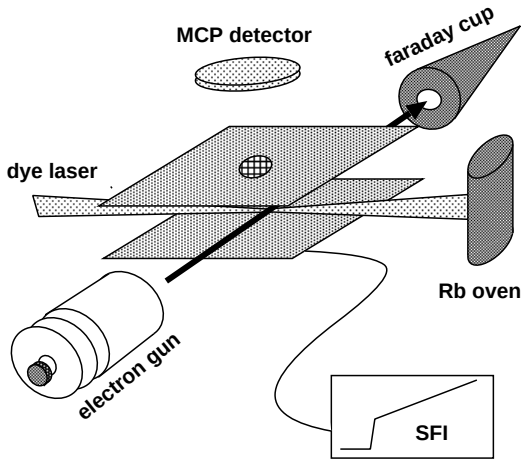

Figure 4.3: Experimental setup for the electron scattering experiment. Rubidium atoms are excited to a Rydberg state around n=30 by a dye laser. Electrons at 680 eV collide with the Rydberg atoms. The resulting transitions are detected by state-selective field ionization. The electron current is measured in a Faraday cup.

electron gun at 680 eV kinetic energy. After traversing the interaction region, where collisions with the Rydberg atoms take place, the beam enters a Faraday cup, where the current is measured with a Keithley 6485 picoammeter.

4.4 Results: SFI traces

In Fig. 4.4 we present SFI traces for the 32s (dashed lines), 31p (dotted lines) and 30d (solid lines) states taken with a linear (a) and a step+linear ramp (b+c) field ramps, respectively and the SFI fields obtained are shown on the right hand side of the figure. The slowly ramped part of the field has a slew rate of 115 V/(cm·μs) in all three cases. In the case of the linear ramp (a), all three states ionize essentially in the same time window. Although each trace displays a complex structure, the SFI profiles do not have any remarkable distinguishing traits. For a SFI ramp that is stepped quickly to 400 V/cm (b), the *s*-state clearly ionizes before the *p* and *d*-states. Furthermore, the *d*-state displays an unique third peak, such that all three states can be distinguished. Another advantagous aspect of SFI fields such as the ones shown in Fig. 4.4b is the reduced time delay between excitation and detection of the Rydberg state, thus reducing background signal from blackbody and collision-induced transitions. In Fig. 4.4c, all the population ionizes during the fast part of the SFI ramp and the SFI profiles of all three states overlap.

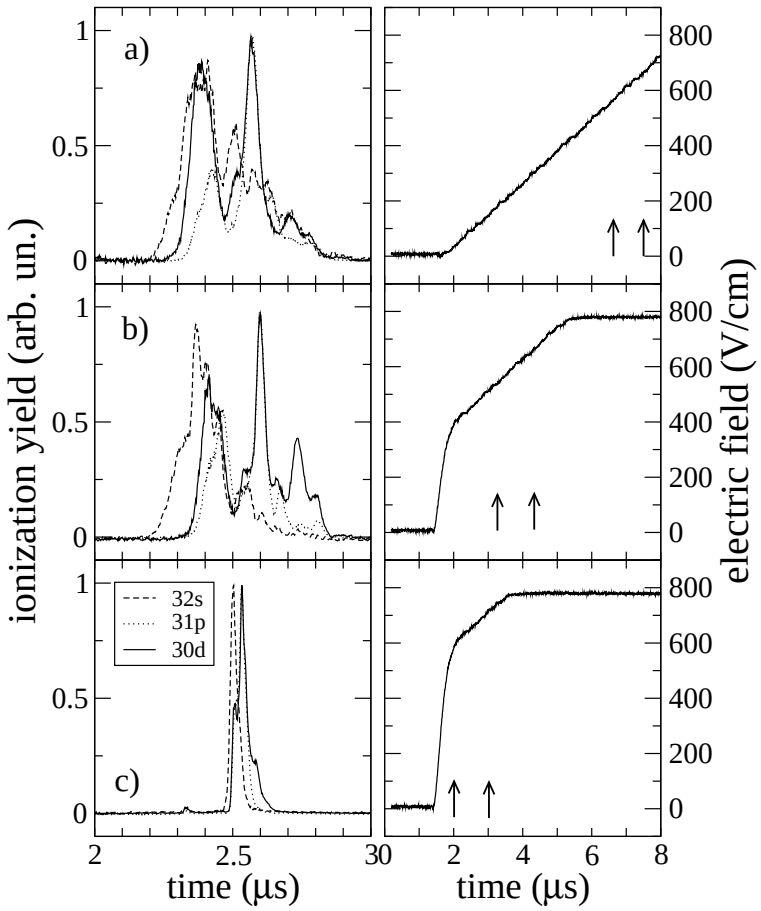

Figure 4.4: SFI profiles for the 32s (dashed), 31p (dotted) and 30d (solid) states of Rb ionized by the field ramps shown on the right. The start and end of the time traces are marked by arrows on the right. For a linear ramp (a), the SFI traces of the three states are difficult to distinguish. For the step in (b), the s state ionizes at much earlier times and the d state has a characteristic third peak. For higher steps (c), all of the states become indistinguishable.

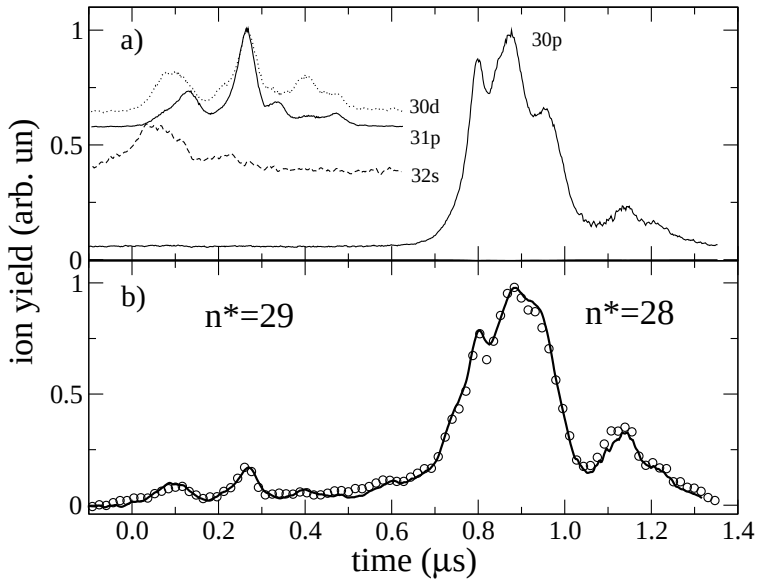

Figure 4.5: a) SFI profile of the initial 30p state. The inset shows SFI traces of the 32s, 31p and 30d states on the same time scale. b) SFI profile after the initial state has been exposed to a 1 μs electron pulse (open dots). The solid line represents a fit to the data using the SFI traces shown in a). Additionally, the traces of the 29d and 31s states were used in the fit.

4.5 Application to collisional excitation with fast electrons

SFI profiles like those shown in Fig. 4.4b offer the possibility to extract the fraction of *s*, *p*, *d* states in a SFI trace of an unknown mixture of the three states since every state has a unique ionization behaviour. If we use the traces shown in Fig. 4.4b as a basis set for a linear combination, we should be able to fit the unknown mixture resulting from an experiment and determine the population in the *s*, *p* and *d* states. In Fig. 4.5a we show the SFI trace of a Rb 30p state. The inset shows the SFI traces of the 32s, 31p and 30d states on the same time scale. In Fig. 4.5b the SFI trace of the initially excited 30p state is shown after exposure to a 1 μs electron pulse with a peak current of 100 μA. Collisions of the electrons with the Rydberg state cause transitions to near-lying states. Transitions to the next higher-lying $n^* = 29$ manifold can be seen as new peaks at small times in Fig. 4.5b. The SFI peak of the 30p state changes in shape, indicating transitions to neighboring $\ell-$states in the same $n^* = 28$ manifold. We fitted a linear combination of the area-normalized SFI traces of the states shown in Fig. 4.5a and the traces of the 29d and 31s states (not shown in the figure) to the trace shown in Fig. 4.5b (solid line). The results of the fit are shown in table 4.1. The

state	% population
32s	1
31p	1
30d	7
31s	10
30p (initial state)	44
29d	37

Table 4.1: State distribution after exposing an initially excited Rb 30p state to a 1 μs electron pulse.

dipole-forbidden transition 30p→31p is, within the noise, not present. The dipole-allowed transition 30p→32s transition is also very weak. As expected, transitions within the same manifold are much stronger than those to the next higher manifold, due to the smaller energy difference between the states.

4.6 Conclusions

We have demonstrated a refined state-selective field ionization technique based on shaped SFI ramps in combination with fitting a linear combination of known SFI traces. This enables us to distinguish between adjacent $\ell-$states in rubidium. The technique is generally applicable and should be able to increase the selectivity of SFI in other atomic and molecular systems as well. The potential of the technique is not exhausted by the step+slow ramp SFI field as used in this chapter. One could imaging a stair-like SFI field with many steps, such that each step ionizes a single Stark state. To obtain the highest selectivity for a given experiment, genetic algorithms and a feedback loop could be used to determine the optimal SFI field shape.

Chapter 5

Imaging of terahertz radiation using a Rydberg atom photocathode

In this chapter we report on a photocathode for far-infrared terahertz (THz) pulses based on ionization of gas-phase Rydberg atoms. We demonstrate the cathode by showing measurements of the beam profile of an unfocused THz beam in the far field of the emitter using an open ion optics and a contact print image of a spatial mask using THz pulse energies of less than 10 nJ. We suggest an improvement based on two-dimensional detection of transitions to near-lying Rydberg states.

5.1 Introduction

Imaging techniques for far-infrared radiation in the terahertz (THz) frequency regime have obtained considerable attention in the last few years. Advances in generation [101, 102] and detection of ultrashort THz pulses with a spectrum from a few GHz to $\sim$2 THz and the interest for non-ionizing radiation for medical and material-probing applications have triggered a fast development of imaging techniques [26, 60]. Most reported THz imaging experiments use lens-coupled semiconductor antennas and focussed weak THz beams. The sample is scanned through the focus and the transmitted or reflected THz pulse shape is measured and used to reconstruct absorption- or phase delay images [43, 59, 60]. Using the temporal profile of a reflected pulse, three-dimensional tomograms have been obtained [59]. Two-dimensional imaging of high-power THz radiation using the electro-optic effect in ZnTe has been demonstrated [99] and used to image moving samples in real time [86]. Very recently, imaging of continuous THz radiation generated by frequency mixing has been accomplished [62]. Developments like the recently demonstrated THz semiconductor-heterostructure laser [47] as well as terahertz parametric generators [46] and oscillators [82] are likely to spur further interest in THz imaging.

In this chapter, we propose an alternative method for two-dimensional imaging of high-power THz pulses based on a Rydberg atom photocathode [23] and show a THz beam profile measured in the far field of a large-aperture GaAs THz emitter as well as a contact print image of a cross-shaped spatial mask.

Atoms in highly excited electronic states, have a weakly bound outer electron with the binding energy given by the Rydberg formula $E_b = -13.6/n^2$ eV where *n* is the principal quantum number [29]. Typical binding energies are 1-100 meV (0.2-24 THz). An external static electric field introduces a saddle point to the atomic potential which lowers the ionization threshold further. The energy barrier is continuously tuneable by choosing the principal quantum number *n* of the Rydberg state and the external field. The upper limit on the sensitivity of the Rydberg atom cathode is set by the minimal binding energy the initial state must retain to be protected from ionization by tunneling and field inhomogeneities.

Although the density of atoms is very low compared with solid-state detectors, Rydberg atoms form a very suitable detector for THz pulses. The ultrashort half-cycle field of the THz pulse with a duration of typically τ_{thz}=0.5 ps is much shorter than the Kepler orbit time τ_K of high Rydberg states, which is in the order of many picoseconds. In the limit $\tau_{\mathrm{thz}} \ll \tau_K$ (impulsive approximation), the THz pulse transfers a momentum $\Delta p = \int E_{\mathrm{thz}}(t)dt$ in atomic units to the Rydberg electron [45]. This leads to an energy change of $\Delta E = p \cdot \Delta p + \frac{\Delta p^2}{2}$, where p is the initial momentum of the Rydberg electron in direction of the THz field. This energy transfer can easily exceed the binding energy of higher lying Rydberg states and it has been shown that a 100% ionization efficiency can be reached at moderate THz field strengths [45].

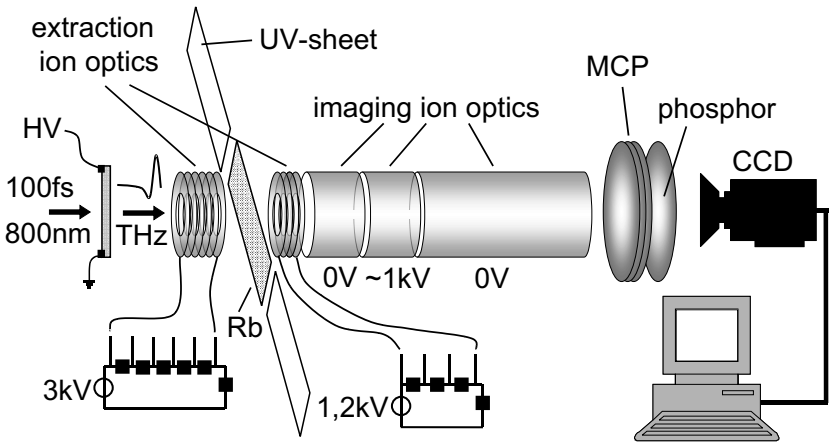

Figure 5.1: Experimental setup. The extraction ion optics create a homogenous field in the plane of the UV light sheet which excites Rb atoms to a Rydberg state. The profile of a THz beam from a large-aperture THz emitter is imprinted on the Rydberg sheet by ionization. The resulting ion distribution is imaged on a MCP detector by an Einzel lens.

5.2 The imaging setup

The experimental setup is shown in Fig. 5.1. To create the photosensitive layer, rubidium is evaporated in an oven heated to 70 °C in a vacuum chamber (10^{-7} mbar). In the interaction plane, a thin film of Rydberg atoms is excited by illuminating Rb atoms with an optical sheet, (height x width) 30 x 1 mm, of ultraviolet light from a frequency doubled nanosecond pulsed dye laser (100 μJ pulse energy) with a repetition rate of 10 Hz . The light at 297.55 nm excites a Stark state in the n=34 manifold in a static electric field of 188 V/cm. As entrance windows we use fused silica for the ultraviolet light and quartz glass for the THz radiation. The THz pulses are generated by a standard biased large-aperture GaAs THz emitter which is illuminated by 800 nm, 100 fs pulses from a regeneratively amplified Ti:Sapphire laser system [101]. The emitter is placed outside the vacuum chamber 25 cm away from the interaction plane.

To permit the entrance of the THz radiation perpendicular to the Rydberg atom sheet while retaining a homogenous electric field in the interaction plane, an open ion optics was designed and simulated with SIMION. The ion optics consists of the extraction optics and a three-element Einzel lens. The extraction optics are composed of two sets of 6 resp. 4 metal rings 50 mm in diameter with 30 mm apertures and spaced by 8 mm. The two sets are spaced by 16 mm. The region between the sets forms the extraction region, in which the Rydberg photocathode is situated. The rings are inter-connected with resistances and biased with a positive voltage such that a linear drop in voltage from left to right in Fig. 5.1 is achieved.

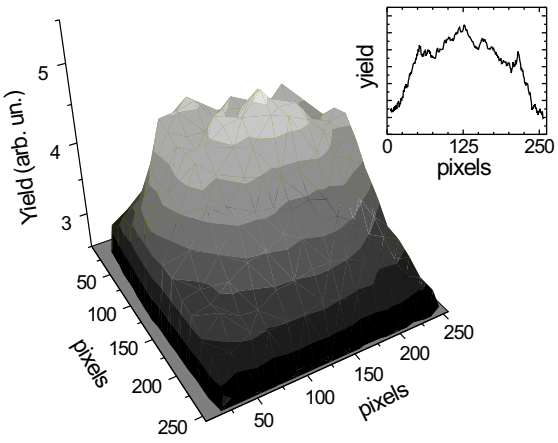

Figure 5.2: Profile of the unfocussed THz beam in the far field 25 cm from the emitter. The inset shows a cut through the center of the profile.

This arrangement creates a homogeneous electric field in the plane of the photosensitive layer while leaving a free entrance for the THz radiation which enters the setup through the left extraction optics in Fig. 5.1 and is imprinted on the Rydberg photocathode by ionization.

The two-dimensional ion distribution resulting from the interaction of the THz pulse with the Rydberg atom sheet is projected on the image plane by a three-element Einzel lens. The Einzel lens compensates for the distortion created in the extraction ion optics. In analogy with light optics a telescope is formed with an objective lens at the end of the extraction ion optics and an ocular in the second cylinder of the Einzel lens. The over-all magnification of the ion optics lens system is ≈ 1.2, depending on the applied voltages. In the image plane a microchannel plate detector (MCP) with a phosphor screen is located. We gate the detection by switching the MCP voltage from 800 to 1800 V. The typical detection window is 300 ns around the mean time of flight of Rb^+ ions created by THz ionization. The obtained images on the phosphor screen are recorded with an 8-bit 256x256 pixel Dalsa camera and stored on a computer for further analysis.

5.3 THz images

In Fig. 5.2 we show the profile of the unfocussed THz beam after 25 cm propagation. The inset shows a single image line from the center of the THz profile image. Clearly, the THz

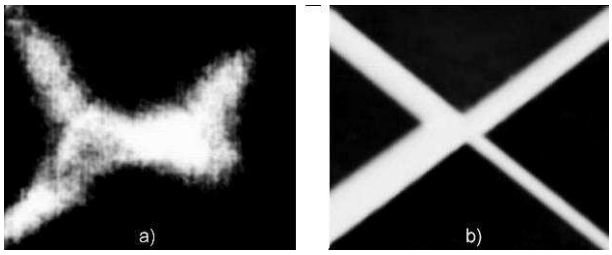

Figure 5.3: Fig: 5.3: a) THz contact print image of a cross-shaped mask placed in front of the extraction region. The thinnest branch of the cross (1 mm) can not be resolved. b) Optical image of the mask.

beam profile is not Gaussian but shows diffraction at the edges of the extraction ion optics. This is due to the divergence of the low frequencies ($\leq$ 300 GHz) in the THz spectrum, which, after 25 cm propagation from the emitter, extend over more than the 3 cm aperture of the ion optics [36].

The number of Rydberg atoms in the 30x30x1 mm^3 interaction region is estimated to be in the order of 10^6. From diffraction calculations and semi-classical simulations of the THz ionization process [34], we estimate a peak THz field of 600 V/cm ($\approx$8 nJ THz pulse energy) and an ionization probability of $\approx$ 7% for the peak THz field strengths in the interaction region. We could take images with THz pulse energies as low as 3 nJ.

In Fig. 5.3a a contact print image of a cross-shaped mask is shown. Fig. 5.3b shows an optical image of the mask. The widths of the branches of the cross are 1, 2, 3 and 4 mm, starting at the lower right branch and counting counterclockwise. The mask is placed as field plate #6 in the extraction ion optics, 8 mm in front of the photocathode. To obtain an image as shown in Fig. 5.3, we take two consequent data sets: An image of the phosphor screen with THz radiation illuminating the mask and a background image with the THz beam blocked. One image is built up in 10 sec by averaging over 100 laser shots. We subtract the background image from the image with THz radiation. The result is shown in Fig 5.3a. Clearly the cross can be seen with the different branches. The lower right branch with a width of 1 mm is not visible due to diffraction. The spectrum of the THz pulses peaks at $\approx$300 GHz, which corresponds to a wavelength of 1 mm. We conclude that the spatial resolution is better than 2 mm, limited by diffraction in the contact-print configuration, i. e. without THz imaging optics.

5.4 Conclusions

In comparison with THz imaging technologies based on THz time-domain spectroscopy (THz-TDS)[43, 59, 60, 86, 99] the Rydberg cathode has advantages as well as disadvantages.

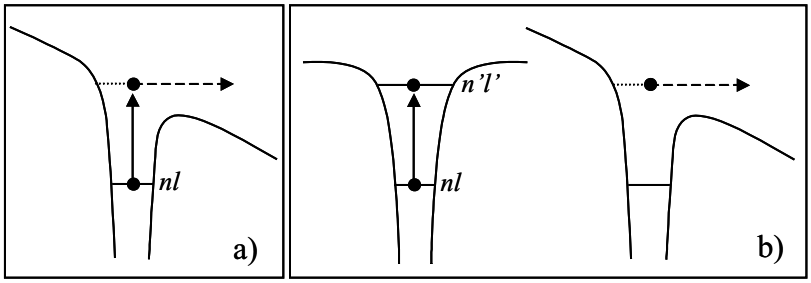

Figure 5.4: Ionization schemes for Rydberg atom photocathodes. (a) Photoionization cathode. The radiation to be imaged (depicted by a solid arrow) ionizes a Rydberg state. The ionized electrons are detected. (b) Pulsed-field cathode.The incoming radiation redistributes the population to a higher-lying Rydberg state. The population in the upper state is then ionized by a pulsed field and detected.

THz-TDS based imaging is phase-sensitive, i. e. measures the temporal THz pulse shape at each image pixel. This allows for phase-retardation images where gradients in refractive index rather than absorption are imaged and extremely high contrast can be obtained. The frequency spectrum at each pixel can provide spectroscopic information. The Rydberg cathode on the other hand can potentially be used for incoherent far-infrared radiation as well as low-power continuous radiation. It is not necessary to overlap femtosecond optical probe and THz pulses in time, which should facilitate imaging of far-away objects and strong absorbers. It should be noted that the image rate can be improved considerably by straightforward technological modifications. Cameras with a higher sensitivity and dye laser systems with higher pulse energies and repetition rates are readily available and will permit single-shot video-rate imaging.

In summary, we used a Rydberg atom photocathode in combination with an open ion optics to image the beam profile of a THz beam in the far field and a contact print of a cross-shaped mask. Rydberg atoms are found to be a suitable and very sensitive photocathode for THz imaging which complements existing THz imaging techniques. The Rydberg photocathode does not require temporal overlap between two ultrashort pulses and is not restricted to coherent radiation.

5.5 Outlook: Pulsed field imaging

In this chapter, we investigated the imaging of ultrashort far-infrared pulses by detecting the electrons ionized by the radiation, as depicted in Fig. 5.4a. Nowadays, promising new sources for tunable narrow-band THz radiation are emerging [14, 46, 47, 82]. In this section we suggest a Rydberg atom photocathode more suited for narrow-band radiation which is

based on bound-bound transitions and subsequent pulsed-field ionization rather than immediate bound-free transitions (see Fig. 5.4b). In this scheme, the incoming radiation excites the Rydberg atoms from an initially populated state $n\ell$ to a higher-lying state $n'\ell'$ in field-free conditions rather than ionize them, and thus imprints the image information in the spatial distribution of higher-lying bound Rydberg states $n'\ell'$. The spatial distribution of the $n'\ell'$ final states can then be probed by applying a fast electric field pulse to the extraction optics instead of using a static field as described earlier in this chapter. The pulsed field serves two purposes: It ionizes the redistributed population and it is then part of the imaging arrangement, providing the fields for the extraction optics.

There are numerous advantages to the pulsed-field imaging scheme: (i) The excitation cross section to a field-free state is generally higher than to a Stark state, such that more Rydberg atoms can be produced. (ii) The cross sections of $\Delta n = 1$ transitions are huge, which can greatly increase the camera's sensitivity for narrow-band radiation. (iii) The photocathode can be made frequency-selective by Stark-tuning. This concept is discussed in greater detail in chapter 6. The restrictions of the pulsed-field scheme lie in the homogeneity and stability of the field produced by the pulsed voltage, and in the thermal movement of the rubidium atoms (in the order of 200 m/s), which thus requires a short time between excitation and ionization.

Chapter 6

Atomic detection of water vapor

We use transitions in rubidium Rydberg atoms as a detector for far-infrared radiation. We can tune the transition frequency by applying an external electric field. By using broad-band far-infrared (terahertz) radiation, we measure the line position and width of the water absorption line at 752 GHz. The interaction of these pulses with Rydberg atoms having a transition which is resonant with an absorbed frequency displays an interesting competition between strong and weak field interaction. We propose an application using Stark-tuned Rydberg atoms as a frequency-selective photocathode for far-infrared imaging.

6.1 Introduction

Spectroscopy in the far-infrared region of the electromagnetic spectrum suffers from two difficulties: sources in the far-infrared are scarce, and detection is hampered by the background from blackbody radiation. Laboratory sources like lamps or microwave-upconverters are typically very weak in the far-infrared [56] whilst lasers are restricted to discrete lines. Very recently, promising new sources in this wavelength regime have been suggested [14, 47]. Detectors are often bolometers which have to be cooled with liquid helium. A powerful method to do spectroscopy in this wavelength region is terahertz time-domain spectroscopy (THz-TDS), which utilizes ultrashort pulses in the THz frequency regime and a coherent detection scheme which is blind to the thermal background [64, 87]. Another efficient detection scheme for far-infrared radiation is based on tuning the transition frequency between two highly excited atomic states by means of an external electric field, i. e. Stark tuning [24]. Rydberg-Rydberg transition frequencies range from radiofrequencies to the far-infrared and their transition moments are large, owing to the similarity of Rydberg wavefunctions with similar principal quantum number n. In this chapter, we employ Stark-tuned Rydberg atoms as a tunable, narrow-band detector for broadband ultrashort far-infrared THz pulses which can be scanned over an absorption line by varying the applied electric field. We discuss the interaction of THz pulses with Rydberg atoms after absorption of discrete frequencies in the THz spectrum by water.

6.2 Stark tuning of transitions

The principle of the detection is depicted in Fig. 6.1. The scheme is based on the fact that Rydberg levels shift in an electric field. The exact energy shift depends on the quantum defect of the involved states. Figure 6.1b shows the Eigenenergies of rubidium Rydberg Stark states around the 25d state as a function of external electric field. The arrow denotes the point where the energy of the dipole transition 25d→28p matches the energy of the 752.033 GHz ($25.085\,\mathrm{cm}^{-1}$) absorption line of water vapor. In part (c) of the figure we show the energy difference between the 25d and 28p states as a function of electric field. Clearly, the transition frequency can be tuned across the water line which has a half width at half maximum of $0.099\,\mathrm{cm}^{-1}$ [74]. Assuming single photon transitions and a constant transition moment over the employed field range, the transition probability to the upper state is a measure for the spectral energy density. It has been shown that the resolution of this detection scheme can be as high as 1 MHz [24].

6.3 Transitions driven by an absorbed frequency

For the ultrashort broadband pulses used in our experiment the situation is more complex and is interesting in itself. In many situations where light and matter interact, the interaction is governed by he spectrum of the light and frequencies of possible transitions of the matter

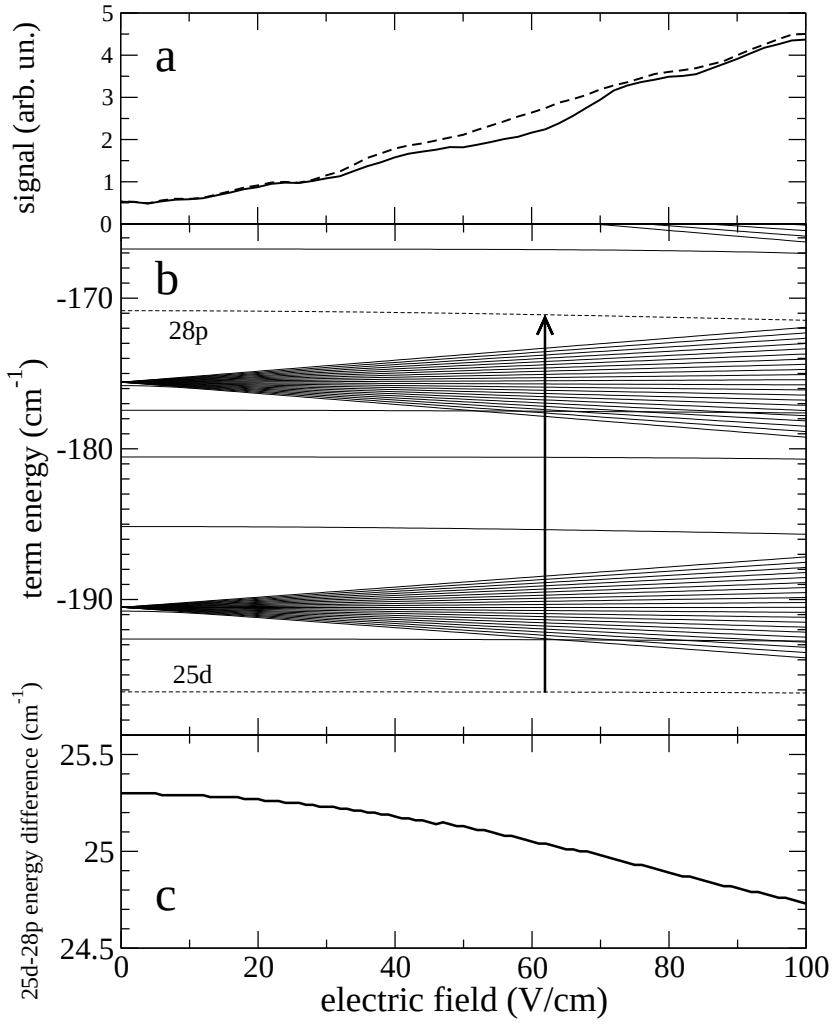

Figure 6.1: (a) 28p state population as a function of external electric field after exposure of an initially excited 25d state to THz pulses which propagated through air containing water vapor (dashed) and dry nitrogen (solid). (b) Rubidium energy levels around the 25d state as a function of electric field. The arrow denotes the field where the 25d-28p transition frequency equals 752 GHz. (c) Energy difference between the Rb 25d and 28p states as a function of field.

in question, which are driven when photons of the matching frequency are absorbed. If the intensity of the light becomes very high, single photon transitions can become less important than the electric field of the light which suppresses the binding Coulomb forces as happens e. g. in above-threshold ionization[1, 28] or in the interaction of Rydberg atoms with strong half-cycle electric field pulses [45, 72, 93, 96]. In other cases, the coherent properties of the light play an important role (for a review, see e. g. [8]). The interaction of Rydberg atoms with terahertz half-cycle pulses which have a spectrum with "gaps" as a result of absorption in gaseous water combines all three of these aspects. The half-cycle field shape of the pulses (which implies large contributions from low frequencies) and the fact that the typical timescales of Rydberg atoms are long compared to the pulse duration of about 0.5 ps make the interaction a strongly driven one which is poorly described by a single-photon picture [85]. This leads to a large contribution of transitions which involve many photons and a complex interaction with the frequencies in the pulse. The absorbed frequencies appear as low-amplitude oscillations in the field shape of the THz pulse which extend for several hundreds of picoseconds after the main pulse. These reshaped pulses have also been observed in N_2O, where the frequency spacing of the rotational absorption lines is almost constant and a periodic rephasing was observed [38, 39].

Figure 6.2a shows the electric field of a pure Gaussian half-cycle pulse with the Fourier transform given in Fig. 6.2b. Pure half-cycle pulses cannot propagate due to their zero-frequency component and develop a slow "tail" of opposite polarity during propagation such that in the far field, the integral of the electric field is zero. The effects of this impurity on Rydberg atom excitation have been investigated earlier and are not taken into account here[84, 93, 96]. THz half-cycle pulses have been used for rotational spectroscopy of multiple molecules in the gas phase [37, 39, 87]. The absorption of frequencies and the following free-induction decay of the excited molecules reshape the THz pulse [3, 39]. The reshaping of the electric field after propagation through a medium which absorbs on discrete lines is for low intensities well described by linear dispersion theory and can be written as [37]

$$\mathcal{E}_{\mathrm{thz}}(z,t) = \int \tilde{\mathcal{E}}_{\mathrm{thz}}(\omega) \cdot e^{-i\omega t + k_0 \cdot z} \cdot e^{i\Delta k z} \cdot e^{-\alpha(\omega) z/2}\, \mathrm{d}\omega$$

where $k = n\omega/c$. $\Delta k(\omega)$ and $\alpha(\omega)$ are the frequency-dependent dispersion and power absorption coefficient, respectively. $\tilde{\mathcal{E}}_{\mathrm{thz}}(\omega)$ is the Fourier transform of the electric field $\mathcal{E}_{\mathrm{thz}}(t)$ of the half-cycle pulse. In the simple single-line absorber model depicted in Fig. 6.2, Δk and α are assumed to have the shape of Lorentzian dispersion- and absorption line shapes. Figure 6.2d shows the frequency spectrum of the half-cycle pulse shown in Fig. 6.2a after propagation through a 40 cm sample of a medium which absorbs on the frequency of the H_2O (J,K_a,K_c)= (2 1 1) ←(2 0 2) transition at 752 GHz [74]. The time-domain pulse shape obtained by an inverse Fourier transform is shown in Fig. 6.2c. The shape of the short half-cycle is not appreciably changed. Following the short half-cycle, there is a low-amplitude oscillatory tail stemming from the free-induction decay of the excited absorber which can extend up to several hundred nanoseconds after the 0.5 ps half-cycle pulse.

Figure 6.1a shows the experimentally determined population in the 28p state as a function

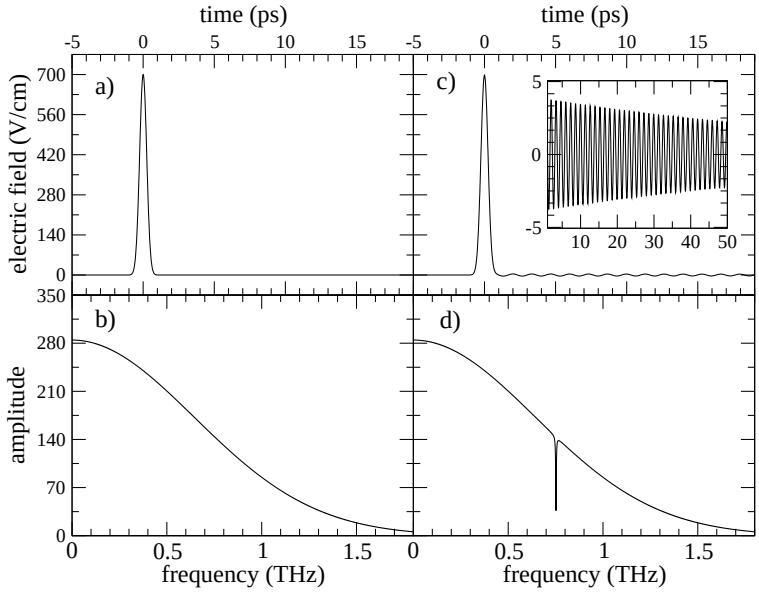

Figure 6.2: Electric field (a) and Fourier transform (b) of a half-cycle pulse with a duration of 0.5 ps. (c) Electric field after propagation through a medium with an absorbing line at 752 GHz calculated by linear dispersion theory. The inset shows a zoom of the low-amplitude oscillatory tail. (d) Frequency spectrum of (c).

of static electric field after an initially excited 25d state was exposed to half-cycle pulses, one which propagated through 40 cm of laboratory air containing water vapour (dashed line) and one which propagated through 40 cm of dry nitrogen (solid line). Surprisingly, at 61 V/cm, when the 25d→28p transition is resonant with the water absorption line at 752 GHz, the pulse which had propagated through water vapour and thus has a hole in the spectrum at this frequency as shown in Fig. 6.2d, transfers *more* population to the upper state than the pulse which propagated through dry nitrogen and has an intact spectrum.

In Fig. 6.3 we show results of an integration of the time-dependent Schrödinger equation of a Rb 25d state in a field as shown in Fig. 6.2a+c. The figure shows the difference in the *p*-state populations for the pulses shown in Fig. 6.2a and c. Obviously, in the field shown in Fig. 6.2c, the missing frequency is present in the temporal field profile, but with a phase shift of π, such that it interferes destructively with the frequency component of the half-cycle pulse, leading to the spectrum shown in 6.2d. In a linear interaction, we would naturally expect that a frequency which is not contained in the spectrum does not drive a transition. The upper state wavefunction excited by the half-cycle pulse would be out of phase with the oscillatory tail and the population is driven back down rather than up, even though the initial

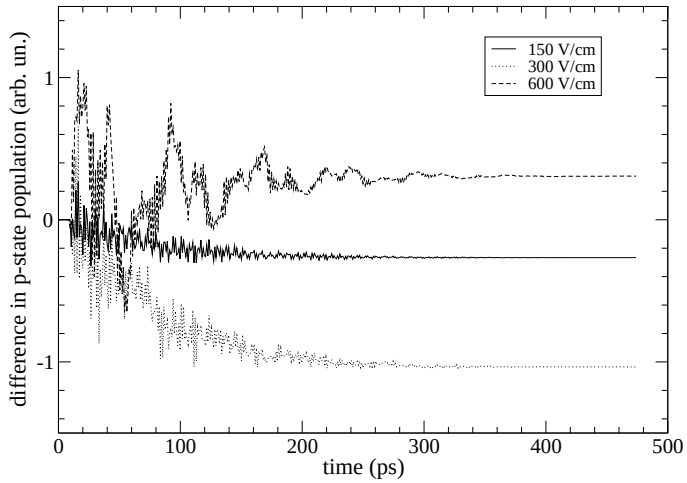

Figure 6.3: Calculated *p*-state population difference between excitation by a THz pulse which propagated through 40 cm of absorbing medium and one which propagated through vacuum for HCP amplitudes of 150 V/cm, 300 V/cm and 600 V/cm.

(25d) state population exceeds the 28p state population by far. This behaviour is shown by the solid and dotted lines in Fig. 6.3 for a 150 V/cm and 300 V/cm half-cycle amplitude. For higher HCP amplitudes, the interaction gains can not be described by an absorption of a single photon anymore. The 28p state population is excited by a multitude of combinations of photos with different energies. As the wavefunction is created by an interplay of many photons of different frequencies (the HCP spectrum contains very low frequencies), the 28p-wavefunction does not have a clear phase relationship with the oscillatory tail any more and this narrow-band feature can efficiently drive more population from the 25d to the 28p state. Naturally, this effect is limited by the fact that such a strong half-cycle pulse leaves very little population in the initial d-state (<10% in the case of the 600 V/cm trace in Fig. 6.3).

This situation can be compared with filtering by linear and nonlinear filters. Linear frequency filters, e. g. dichroic bandpass filters [98], will produce a gap in the spectrum when applied to a pulse like the one shown in Fig. 6.2c. Nonlinear filters, e. g. ultrafast switchable mirrors switched on after the HCP [84], can produce a pulse with a *peak* at the absorbed frequency. This might be a convenient way to generate narrow-band radiation on absorption lines of molecules for spectroscopic applications.

Small polar molecules such as water have strong rotational transitions in the far-infrared. In Fig. 6.4, we show some strong absorption lines of water in the frequency region between 0.3 and 1.2 THz taken from the HITRAN database [74], which includes the JPL submillimeter, millimeter, and microwave spectral line catalog [67]. The thickness of the lines gives a rough

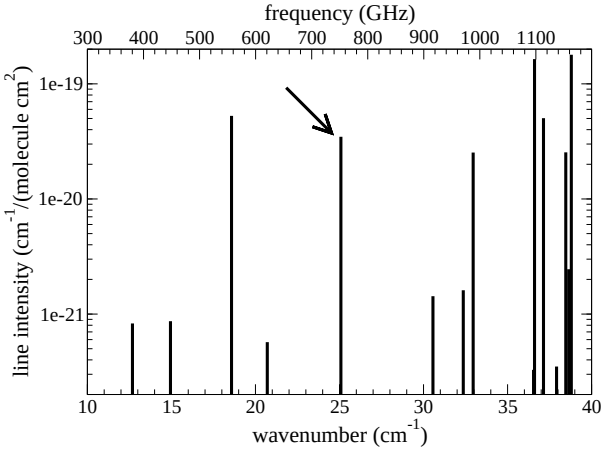

Figure 6.4: Line intensities for some strong water absorption lines in the far-infrared (0.3-1.2 THz). The line chosen for the experiments is marked with an arrow.

estimate of the actual line widths. For the measurements presented in this chapter, we chose a strong water absorption line at 752 GHz (marked with an arrow). The method is generally applicable. To find the best transition and field strength to use in the experiment, Stark level maps similar to the one shown in Fig. 6.1b were calculated for a number of n states of rubidium and searched for matching transitions by a computer algorithm. To widen the range of detectable frequencies, the search can easily be extended to other atomic systems.

6.4 Experimental setup

The experimental setup is sketched in Fig. 6.5. The experiment is performed in a vacuum chamber (10^{-7} mbar). A collimated beam of rubidium atoms from a resistively heated oven is excited to the 25d state in a non-resonant two-photon process by a dye laser which is focussed between two capacitor plates. The excitation takes place in a variable electric field. The static electric field is produced by a voltage of 0-200 V supplied by a computer-controlled power supply, and which is applied to one of the capacitor plates. Counter-propagating to the dye laser, the THz beam enters the chamber through a quartz-glass window. The THz beam is generated by a standard biased large-aperture semiconductor antenna [42, 101]. Briefly, a 100 fs, 800 nm pulse illuminates a semi-insulating GaAs wafer which is biased with a pulsed high voltage. The absorbed photons lift carriers from the valence band to the conduction band. The carriers are accelerated by the bias voltage and radiate an ultrashort electromagnetic pulse with a frequency spectrum ranging from 100 GHz to $\sim$2 THz. The interaction of the

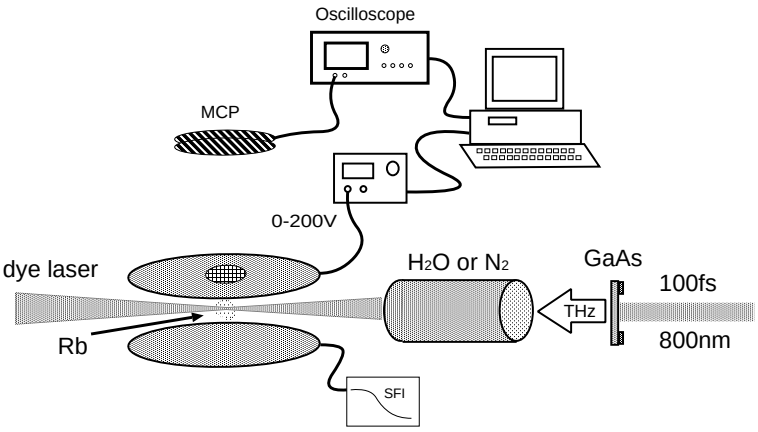

Figure 6.5: Experimental setup. Rubidium atoms excited to the 25d state by a dye laser are subjected to a THz pulse which propagates through a tube filled with air containing water vapor or dry nitrogen. The Rydberg state distribution is determined by means of state-selective field ionization (SFI).

THz radiation with the Rydberg atoms causes transitions to near-lying states. The final state distribution after the THz interaction is determined by means of state-selective field ionization (SFI). To that end, a slowly ramped electric field is applied to the second capacitor plate. The field needed to ionize a Rydberg state of principal quantum number n scales as n^{-4} , such that the field at which a state ionizes is a measure for the state's principal quantum number n [29]. The SFI field also pushes the ionized electrons towards a microchannel plate detector (MCP). The time-of-flight at which the electrons arrive gives the ionization field and, with it, the state distribution. The MCP signal is digitized by a fast digital oscilloscope and the traces are stored on a computer for further processing.

Before entering the vacuum chamber, the THz beam traverses a 25 cm tube which can be filled with air containing water vapor or flooded with dry nitrogen. To measure a line profile as shown in Fig. 6.1a, the SFI traces are taken after exposing the Rydberg atoms to the THz beam which propagated through the tube containing water vapor. Then the static electric field is increased and the next trace is taken. The field scan is then repeated with the THz beam blocked to account for long-term drifts, for example in the oven temperature. To improve statistics, this procedure is repeated several times. Then the water vapor tube is flooded with dry nitrogen and the measurement is repeated. The absorption data is then the difference in upper state population for the water vapor and nitrogen data, respectively.

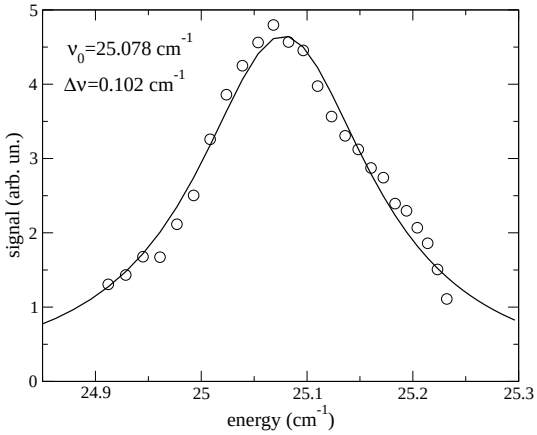

Figure 6.6: Measured absorption line profile of the H_2O (J,K_a,K_c)= (2 1 1) ←(2 0 2) transition (open circles). The line represents a Voigt profile fit to the data. The *x*-axis is converted from field to wavenumber using Fig. 6.1c.

6.5 Results

In Fig. 6.6, we show the measured line shape of the H_2O (J,K_a,K_c)= (2 1 1) ←(2 0 2) transition at 752 GHz. The line shape is obtained by plotting the difference in transition probability to the upper state for a THz pulse which propagated through air containing water vapor and a reference pulse which propagated through dry nitrogen as a function of energy separation of the 25d and 28p states. The field-to-frequency conversion is provided by Fig. 6.1c. Figure 6.6 shows the experimental water line data as a function of frequency (circles) along with a Voigt profile fit to the data (solid line). The values for the water line extracted from the fit are the line position at $\nu_0 = 25.078\,\mathrm{cm}^{-1}$ with a half-width half-maximum of $\Delta\nu = 0.0102\,\mathrm{cm}^{-1}$. These values are in good agreement with line data from the HITRAN spectroscopic database: ν_0 =25.085 cm^{-1}, $\Delta\nu$ =0.099 cm^{-1} [74]. Uncertainties in the line position and width arise mainly from the error in the determination of the electric field and field inhomogeneities. The gradient of the curve plotted in Fig. 6.1c around 60 V/cm is about 0.008 $\mathrm{cm}^{-1}/(\mathrm{V/cm})$. We estimate our error in field to be on the order of 2%, yielding an error in line position of $\sim 0.01\,\mathrm{cm}^{-1}$. Other sources of error are the accuracy of the level map calculation and fluctuations in the THz and dye laser intensity.

6.6 Outlook and conclusions

The spectroscopic technique presented here is, despite its potentially very high resolution, not likely to be applied in high-resolution spectroscopy as it requires prior knowledge of the approximate line position to determine which atom, Rydberg state and fields to be used. The main value of the technique lies in using known absorption lines of small polar molecules to detect the presence of these molecules in a gas-air mixture. In Chapter 5 of this thesis an imaging camera was demonstrated which employs Rydberg atoms as a photosensitive layer for THz pulses [33]. This far-infrared camera made use of the low ionization potential of Rydberg atoms in an electric field. The camera can be made frequency-selective using Stark-tuning of Rydberg states well beneath the ionization limit and two-dimensional detection of pulsed-field ionization of the upper state Rydberg atoms. In this way, the redistributed rather than the ionized Rydberg states can be imaged (see section 5.5). This will make it possible to image gas concentrations in the far-infrared region in real time. Preliminary experiments towards that end were successful.

In conclusion, we used Stark-tuned Rydberg atoms and broadband THz pulses to detect the presence of water vapor and measure a water absorption line in the far infrared. The experimental results are in good agreement with published database values. We suggest an application in frequency-selective far-infrared imaging using Rydberg atom photocathodes.

Appendix A

Integration of the classical equation of motion

The equation of motion of the classical atomic model, an electron in the Coulomb field of the atomic core, is the Kepler equation (given in atomic units):

$$\ddot{\vec{r}} = -\frac{\overrightarrow{r}}{r^3}. \tag{A.1}$$

The solutions of Eq. (A.1) are ellipses with the atomic core in one focal point as depicted in Fig. 1.1. The classical equation of motion (A.1) must be combined with initial conditions derived from quantum mechanics. A stationary Rydberg state is described by the quantum numbers *n*, *l*, *m*, which give the state's energy, angular momentum and its projection on the quantization axis. The energy of the initial state is given by the Rydberg formula

$$E_n = -\frac{1}{2(n-\delta_\ell)^2}. \tag{A.2}$$

E_n determines the major axis a of the ellipse. The angular momentum determines the minor axis (Sommerfeld quantization condition). This leads to

$$a = n^2 \tag{A.3}$$

$$b = \frac{a}{n} l \quad , \; l = \frac{1}{2} \ldots n - \frac{1}{2} \tag{A.4}$$

To solve the equation of motion, we let the electron start at the inner turning point of the ellipse. The initial conditions for the radial coordinate r and the velocity v read

$$|\vec{r}_0| = r_{min} = a - \sqrt{a^2 - b^2} \tag{A.5}$$

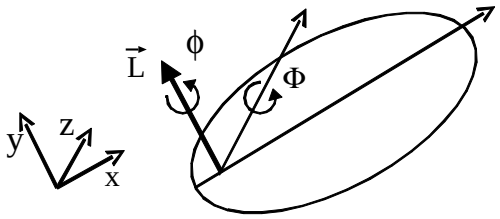

Figure A.1: Two undefined degrees of freedom in the initial conditions.

$$|\vec{v}_0| = 2\sqrt{-\frac{1}{2n^2} + \frac{1}{r_{min}}} \tag{A.6}$$

For a twodimensional description, the initial conditions are hereby given. For calculations in a magnetic field, a three-dimensional model is needed. In three dimensions, the directions of $\vec{r}_0$ and $\vec{v}_0$ are defined by

$$\vec{L} \cdot \vec{v}_0 = 0 \qquad \vec{L} \cdot \vec{r}_0 = 0 \tag{A.7}$$

$$\vec{v}_0 \cdot \vec{r}_0 = 0 \tag{A.8}$$

where the angular momentum $\vec{L}$ is given by

$$|\vec{L}| = l \qquad \vec{L} \cdot \hat{e}_z = m \tag{A.9}$$

$\vec{L}$ is the angular momentum of the orbit and $\hat{e}_z$ is the unit vector in *z* direction, which is chosen as the quantization axis. With Eq. (A.5)-(A.9), the equation of motion can easily be integrated numerically, e. g. by a Runge-Kutta algorithm with adaptive stepsize [69]. An algorithm with adaptive time step size is mandatory, as the velocity of the electron can easily vary over 4 orders of magnitude on different parts of its orbit.

Equations (A.5)-(A.9) for $\vec{r}_0$, $\vec{v}_0$ and $\vec{L}$ leave two degrees of freedom undefined. This is illustrated in Fig. A.1. Rotations around the $\vec{L}$- and the quantization axis $\hat{e}_z$ do not change the values of *n,l,m* for this orbit. Therefore a classical translation of a quantum mechanical ensemble with the same *n,l,m*, is an average over randomly chosen rotation angles ϕ and Φ. The Runge-Lenz vector, i. e. the direction of the major axis in space, is only conserved for a pure $1/r$-potential, which is only found in atomic hydrogen. In any other atom, the Runge-Lenz vector will precess, depending in the quantum defect of the state.

Having chosen a random orbit which complies to *n*, *l*, *m* there is one more quantum mechanical property of the initial state which can be accounted for: the angular probability distribution of the QM state given by the square of the angular wavefunction, which is proportional to the square of the spherical harmonic $|Y_{lm}(\theta, \varphi)|^2$ for the appropriate *l* and *m*. This can be done using the rejection method [69].

Bibliography

[1] P. Agostini, F. Fabre, G. Mainfray, G. Petite, and N. K. Rahman. Free-free transitions following six-photon ionization of xenon atoms. *Phys. Rev. Lett.* **42**, 1127 (1979).

[2] J. Ahn, T. C. Weinacht, and P. H. Bucksbaum. Information storage and retrieval through quantum phase. *Science* **287**, 463 (2000).

[3] L. Allen and J. H. Eberly. *Optical resonance and two-level atoms*. John Wiley & Sons, Inc., New York, 1975.

[4] Ph. Antoine, A. L'Huillier, and M. Lewenstein. Attosecond pulse trains using high order harmonics. *Phys. Rev. Lett.* **77**, 1234 (1996).

[5] A. Baltuška et al. Attosecond control of electronic processes by intense light fields. *Nature* **421**, 611 (2003).

[6] M. C. Baruch and T. F. Gallagher. Angular distribution of electrons from low-frequency above-threshold ionization. *Phys. Rev. A* **44**, 5803 (1991).

[7] D. Bauer and P. Mulser. Exact field ionization rates in the barrier-suppression regime from numerical time-dependent Schrödinger-equation calculations. *Phys. Rev. A* **59**, 569 (1999).

[8] K. Bergmann, H. Theuer, and B. W. Shore. Coherent population transfer among quantum states of atoms and molecules. *Rev. Mod. Phys.* **70**, 1003 (1998).

[9] Hans A. Bethe and Edwin E. Salpeter. *Quantum mechanics of one- and two-electron atoms*. Springer Verlag, Berlin, 1957.

[10] R. Bradley, J. Clarke, D. Kinion, L. J. Rosenberg, K. van Bibber, S. Matsuki, M. Mück, and P. Sikivie. Microwave cavity searches for dark-matter axions. *Rev. Mod. Phys.* **75**, 777 (2003).

[11] T. Brixner, N. H. Damrauer, P. Niklaus, and G. Gerber. Photoselective adaptive femtosecond quantum control in the liquid phase. *Nature* **414**, 57 (2001).

[12] T. Brixner, A. Oehrlein, M. Strehle, and G. Gerber. Feedback-controlled femtosecond pulse shaping. *Applied Physics B* **70**, S119 (2000).

[13] A. Bugacov, B. Piraux, M. Pont, and R. Shakeshaft. Ionization of Rydberg hydrogen by a half-cycle pulse. *Phys. Rev. A* **51**, 1490 (1995).

[14] G. L. Carr, M. C. Martin, W. R. McKinney, K. Jordan, G. R. Neil, and G. P. Williams. High-power terahertz radiation from relativistic electrons. *Nature* **420**, 153 (2002).

[15] S. Chelkowski and A. D. Bandrauk. Sensitivity of spatial distributions to the absolute phase of an ultrashort intense laser pulse. *Phys. Rev. A* **65**, 061802 (2002).

[16] Y. W. Choi, M. D. Bowden, and K. Muraoka. Electric field measurements in an argon glow discharge using laser spectroscopy. *Appl. Phys. Lett.* **69**, 1361 (1996).

[17] I. P. Christov. Phase-dependent loss due to nonadiabatic ionization by sub-10-fs pulses. *Opt. Lett.* **24**, 1425 (1999).

[18] P. B. Corkum. Plasma perspective on strong-field multiphoton ionization. *Phys. Rev. Lett.* **71**, 1994 (1993).

[19] P. B. Corkum, N. H. Burnett, and F. Brunel. Above-threshold ionization in the long-wavelength limit. *Phys. Rev. Lett.* **62**, 1259 (1989).

[20] A. de Bohan, P. Antoine, D. B. Milošević, and B. Piraux. Phase-dependent harmonic emission with ultrashort laser pulses. *Phys. Rev. Lett.* **81**, 1837 (1998).

[21] H.-J. Dietrich, K. Müller-Dethlefs, and L. Ya. Baranov. Fractional stark state selective electric field ionization of very high-*n* Rydberg states of molecules. *Phys. Rev. Lett.* **76**, 3530 (1996).

[22] M. Drabbels and L. D. Noordam. A streak camera operating in the mid-infrared. *Opt. Lett.* **22**, 1436 (1997).

[23] M. Drabbels and L. D. Noordam. Infrared imaging camera based on a Rydberg atom photodetector. *Appl. Phys. Lett.* **74**, 1797 (1999).

[24] T. W. Ducas, William P. Spencer, A. G. Vaidyanathan, W. H. Hamilton, and D. Kleppner. Detection of far-infrared radiation using Rydberg atoms. *Appl. Phys. Lett.* **35**, 382 (1979).

[25] U. Fano, F. Robicheaux, and A. R. P. Rau. Semianalytic study of diamagnetism in a degenerate hydrogenic manifold. *Phys. Rev. A* **37**, 3655 (1988).

[26] B. Ferguson and X.-C. Zhang. Materials for terahertz science and technology. *Nature Materials* **1**, 26 (2002).

[27] G. W. Foltz, E. J. Beiting, T. H. Jeys, K. A. Smith, F. B. Dunning, and R. F. Stebbings. State changing in Na(nd)-eletron collisions. *Phys. Rev. A* **25**, 187 (1982).

[28] T. F. Gallagher. Above-threshold ionization in low-frequency limit. *Phys. Rev. Lett.* **61**, 2304 (1988).

[29] T. F. Gallagher. *Rydberg Atoms*. Cambridge University Press, Cambridge, 1994.

[30] T. F. Gallagher and W. E. Cooke. The detection of 300 °K blackbody radiation with Rydberg atoms. *Appl. Phys. Lett.* **34**, 369 (1979).

[31] T. F. Gallagher, L. M. Humphrey, R. M. Hill, and S. A. Edelstein. Resolution of $|m_l|$ and $|m_j|$ levels in the electric field ionization of highly excited d states of Na. *Phys. Rev. Lett.* **37**, 1465 (1976).

[32] T. F. Gallagher, B. E. Perry, K. A. Safinya, and W. Sandner. Spin-orbit effect in the electric field ionization of Rb and Cs. *Phys. Rev. A* **24**, 3249 (1981).

[33] A. Gürtler, A. S. Meijer, and W. J van der Zande. Imaging of terahertz radiation using a Rydberg atom photocathode. *Appl. Phys. Lett.* **83**, 222 (2003).

[34] A. Gürtler, A. S. Meijer, and W. J van der Zande. Terahertz imaging with Rydberg atom photocathodes. unpublished, 2003.

[35] A. Gürtler, M. J. J. Vrakking, W. J. van der Zande, and L. D. Noordam. Carrier phase dependence in the ionization of Rydberg atoms by short radiofrequency pulses, a model system for high order harmonic generation. Submitted to Phys. Rev. Lett., 2003.

[36] A. Gürtler, C. Winnewisser, H. Helm, and P. U. Jepsen. Terahertz pulse propagation in the near field and the far field. *J. Opt. Soc. Am. A* **17**, 74 (2000).

[37] H. Harde, R. A. Cheville, and D. Grischkowsky. Terahertz studies of collision-broadened rotational lines. *J. Phys. Chem. A* **101**, 3646 (1997).

[38] H. Harde and D. Grischkowsky. Coherent transients excited by subpicosecond pulses of THz radiation. *J. Opt. Soc. Am. B* **8**, 1642 (1991).

[39] H. Harde, S. Keiding, and D. Grischkowsky. THz commensurate echoes: Periodic rephasing of molecular transitions in free-induction decay. *Phys. Rev. Lett.* **66**, 1834 (1991).

[40] David A. Harmin. Coherent time evolution on a grid of Landau-Zener anticrossings. *Phys. Rev. A* **56**, 232 (1997).

[41] D. R. Hartree. *Proc. Cambridge Phil. Soc* **24**, 89 (1928).

[42] B. B. Hu, J. T. Darrow, X.-C. Zhang, and D. H. Auston. Optically steerable photoconducting antennas. *Appl. Phys. Lett.* **56**, 886 (1990).

[43] B B Hu and M C Nuss. Imaging with THz waves. *Opt. Lett.* **20**, 1716 (1995).

[44] R. R. Jones. Creating and probing electronic wave packets using half-cycle pulses. *Phys. Rev. Lett.* **76**, 3927 (1996).

[45] R. R. Jones, D. You, and P. H. Bucksbaum. Ionization of Rydberg atoms by subpicosecond half-cycle pulses. *Phys. Rev. Lett.* **70**, 1236 (1993).

[46] K. Kawase, J. Shikata, K. Imai, and H. Ito. Transform-limited, narrow-linewidth, terahertz-wave parametric generator. *Appl. Phys. Lett.* **78**, 2819 (2001).

[47] R. Köhler, A. Tredicucci, F. Beltram, H. E. Beere, E. H. Linfield, A. G. Davies, D. A. Ritchie, R. C. Iotti, and F. Rossi. Terahertz semiconductor-heterostructure laser. *Nature* **417**, 156 (2002).

[48] D. Kleppner, M. G. Littman, and M. L. Zimmerman. Rydberg atoms in strong fields. In R. F. Stebbings and F. B. Dunning, editors, *Rydberg states of atoms and molecules*, chapter 3. Cambridge University Press, 1983.

[49] J. L. Krause, K. J. Schafer, and K. C. Kulander. High-order harmonic generation from atoms and ions in the high intensity regime. *Phys. Rev. Lett.* **68**, 3535 (1992).

[50] P. Kruit and F. H. Read. Magnetic-field parallelizer for 2-π-electron spectrometer and electron-image magnifier. *J. Phys. E* **16**, 313 (1983).

[51] P. Lambropoulos. Mechanisms for multiple ionization of atoms by strong pulsed lasers. *Phys. Rev. Lett.* **55**, 2141 (1985).

[52] A. L'Huillier and Ph. Balcou. High-order harmonic generation in rare gases with a 1-ps 1053-nm laser. *Phys. Rev. Lett.* **70**, 774 (1993).

[53] W. Li, I. Mourachko, M. W. Noel, and T. F. Gallagher. Millimeter-wave spectroscopy of cold Rb Rydberg atoms in a magneto-optical trap: Quantum defects of the ns, np, and nd series. *Phys. Rev. A* **67**, 052502 (2003).

[54] C.-J. Lorenzen and K. Niemax. Quantum defects of the $n\ ^2p_{1/2,3/2}$ levels in ^{39}K I and ^{85}Rb I. *Physica Scripta* **27**, 300 (1983).

[55] C. R. Mahon, J. L. Dexter, P. Pillet, and T. F. Gallagher. Ionization of sodium and lithium Rydberg atoms by 10-MHz to 15-GHz electric fields. *Phys. Rev. A* **44**, 1859 (1991).

[56] D. H. Martin, editor. *Spectroscopic techniques for far infra-red, submillimetre and millimetre waves*. North-Holland Publishing Company, Amsterdam, 1967.

[57] H. J. Metcalf and P. van der Straten. *Laser cooling and trapping*. Springer Verlag, Berlin, 1999.

[58] D. B. Milošević, G. G. Paulus, and W. Becker. Phase-dependent effects of a few-cycle laser pulse. *Phys. Rev. Lett.* **89**, 153001 (2002).

[59] D. M. Mittleman, S. Hunsche, L. Boivin, and M. C. Nuss. T-ray tomography. *Opt. Lett.* **22**, 904 (1997).

[60] D. M. Mittleman, R. H. Jacobsen, and M C. Nuss. T-ray imaging. *IEEE J. Sel. Top. Quant. El.* **2**, 679 (1996).

[61] P. J. Mohr and B. N. Taylor. CODATA recommended values of the fundamental physical constants: 1998. *Rev. Mod. Phys.* **72**, 351 (2000). http://physics.nist.gov/constants.

[62] A. Nahata, J. T. Yardley, and T. F. Heinz. Two-dimensional imaging of continous-wave terahertz radiation using electro-optic detection. *Appl. Phys. Lett.* **81**, 963 (2002).

[63] L. D. Noordam and R. R. Jones. *Electronic wavepackets*, volume 38 of *Advances in atomic, molecular and optical physics*, chapter 1. Academic Press, San Diego, 1998.

[64] M. C. Nuss and J. Orenstein. THz time-domain spectroscopy. In George Grüner, editor, *Millimeter wave spectroscopy of solids*. Springer, 1996.

[65] P. M. Paul, E. S. Toma, P. Breger, G. Mullot, F. Augé, Ph. Balcou, H. G. Muller, and P. Agostini. Observation of a train of attosecond pulses from high harmonic generation. *Science* **292**, 1689 (2001).

[66] G. G. Paulus, F. Grasbon, H. Walther, P. Villoresi, M. Nisoli, S. Stagira, E. Priori, and S. de Silvestri. Absolute-phase phenomena in photoionization with few-cycle laser pulses. *Nature* **414**, 182 (2001).

[67] H. M. Pickett, R. L. Poynter, E. A. Cohen, M. L. Delitsky, J. C. Pearson, and H. S. P. Muller. Submillimeter, millimeter, and microwave spectral line catalog. *J. Quant. Spect. & Rad. Trans.* **60**, 883 (1998). (http://spec.jpl.nasa.gov/).

[68] J. H. Posthumus, A. J. Giles, M. R. Thompson, and K. Codling. Field-ionization, coulomb explosion of diatomic molecules in intense laser fields. *J. Phys. B* **29**, 5811 (1996).

[69] William H. Press, Saul A. Teukolsky, William T. Vetterling, and Brian P. Flannery. *Numerical Recipes in C*. Cambridge University Press, Cambridge, 1992.

[70] C. Rangan, K. J. Schaefer, and A. R. P. Rau. Dynamics of diamagnetic Zeeman states ionized by half-cycle pulses. *Phys. Rev. A* **61**, 053410 (2000).

[71] C. O. Reinhold, M. Melles, H. Shao, and J. Burgdörfer. Ionization of Rydberg atoms by half-cycle pulses. *J. Phys. B* **26**, L659 (1993).

[72] F. Robicheaux. Pulsed field ionization of Rydberg atoms. *Phys. Rev. A* **56**, R3358 (1997).

[73] F. Robicheaux, C. Wesdorp, and L. D. Noordam. Selective field ionization in Rb and Li: Theory and experiment. *Phys. Rev. A* **62**, 043404 (2000).

[74] L. S. Rothman et al. The HITRAN molecular spectroscopic database and HAWKS (HITRAN Atmospheric Workstation): 1996 edition. *J. Quant. Spect. & Rad. Trans.* **60**, 665 (1998). http://cfa-www.harvard.edu/HITRAN/.

[75] B. E. Sauer, S. Yoakum, L. Moorman, and P. M. Koch. Dynamic tunneling ionization of excited hydrogen atoms: A precise experiment versus theories. *Phys. Rev. Lett.* **68**, 468 (1992).

[76] K. J. Schafer and K. C. Kulander. High harmonic generation from ultrafast pump lasers. *Phys. Rev. Lett.* **78**, 638 (1997).

[77] V. Schyja, T. Lang, and H. Helm. Channel switching in above-threshold ionization of xenon. *Phys. Rev. A* **57**, 3692 (1998).

[78] B. Sheehy, J. D. D. Martin, L. F. DiMauro, P. Agostini, K. J. Schafer, M. B. Gaarde, and K. C. Kulander. High harmonic generation at long wavelengths. *Phys. Rev. Lett.* **83**, 5270 (1999).

[79] R. F. Stebbings and F. B. Dunning, editors. *Rydberg states of atoms and molecules*. Cambridge University Press, 1983.

[80] X. Sun and K. B. MacAdam. Angular-momentum distribution following impact of slow ions on Na(nd) Rydberg atoms. *Phys. Rev. A* **47**, 3913 (1993).

[81] M. Tada, Y. Kishimoto, M. Shibata, K. Kominato, S. Yamada, T. Haseyama, I. Ogawa, H. Funahashi, K. Yamamoto, and S. Matsuki. Manipulating ionization path in a Stark map: Stringent schemes for the selective field ionization in highly excited Rb Rydberg atoms. *Phys. Lett. A* **303**, 285 (2002).

[82] T. Tanabe, K. Suto, J. Nishizawa, K. Saito, and T. Kimura. Tunable terahertz wave generation in the 3- to 7-THz region from GaP. *Appl. Phys. Lett.* **83**, 237 (2003).

[83] G. Tempea, M. Geissler, and T. Brabec. Phase sensitivity of high-order harmonic generation with few-cycle laser pulses. *J. Opt. Soc. Am. B* **16**, 669 (1999).

[84] N. E. Tielking, T. J. Bensky, and R. R. Jones. Effects of imperfect unipolarity on the ionization of Rydberg atoms by subpicosecond half-cycle pulses. *Phys. Rev. A* **51**, 3370 (1995).

[85] N. E. Tielking and R. R. Jones. Coherent population transfer among Rydberg states by subpicosecond, half-cycle pulses. *Phys. Rev. A* **52**, 1371 (1995).

[86] M. Usami, T. Iwamoto, R. Fukasawa, M. Tani, M. Watanabe, and K. Sakai. Development of a THz spectroscopic imaging system. *Phys. Med. Biol.* **47**, 3749 (2002).

[87] M. van Exter, Ch. Fattinger, and D. Grischkowsky. Terahertz time-domain spectroscopy of water vapor. *Opt. Lett.* **14**, 1128 (1989).

[88] J. B. M. Warntjes, A. Gürtler, A. Osterwalder, F. Roşca-Prună, M. J. J. Vrakking, and L. D. Noordam. Atomic spectral detection of tunable extreme ultraviolet pulses. *Opt. Lett.* **26**, 1463 (2001).

[89] J. B. M. Warntjes, A. Gürtler, A. Osterwalder, F. Roşca-Prună, M. J. J. Vrakking, and L. D. Noordam. Atomic streak camera operating in the extreme ultraviolet. *Rev. Sci. Instr.* **72**, 3205 (2001).

[90] R. B. Watkins, W. M. Griffith, M. A. Gatzke, and T. F. Gallagher. Multiphoton resonance with one to many cycles. *Phys. Rev. Lett.* **77**, 2424 (1996).

[91] T. C. Weinacht, J. Ahn, and P. H. Bucksbaum. Controlling the shape of a quantum wavefunction. *Nature* **397**, 233 (1999).

[92] A. M. Weiner. Femtosecond pulse shaping using spatial light modulators. *Rev. Sci. Instr.* **71**, 1929 (2000).

[93] C. Wesdorp, F. Robicheaux, and L. D. Noordam. Displacing Rydberg electrons: The mono-cycle nature of half-cycle pulses. *Phys. Rev. Lett.* **87**, 083001 (2001).

[94] C. Wesdorp, F. Robicheaux, and L. D. Noordam. Pulsed field recombination. *Phys. Rev. A* **64**, 033414 (2001).

[95] A. Wetzels, A. Gürtler, A. Buijserd, T. Vijftigschild, H. ter Horst, and W. J. van der Zande. Reduction of electronic noise in THz generation. *Rev. Sci. Instr.* **74**, 3180 (2003).

[96] A. Wetzels, A. Gürtler, L. D. Noordam, F. Robicheaux, C. Dinu, H. G. Muller, M. J. J. Vrakking, and W. J. van der Zande. Rydberg state ionization by half-cycle-pulse excitation: Strong kicks create slow electrons. *Phys. Rev. Lett.* **89**, 273003 (2002).

[97] A. A. R. Wetzels, A. Gürtler, H. G. Muller, and L. D. Noordam. The dynamics of a THz Rydberg wavepacket. *Eur. Phys. J. D* **14**, 157 (2001).

[98] C. Winnewisser, F. Lewen, and H. Helm. Transmission characteristics of dichroic filters measured by THz time-domain spectroscopy. *Appl. Phys. A* **66**, 593 (1998).

[99] Q. Wu, T. D. Hewitt, and X.-C. Zhang. Two-dimensional electro-optic imaging of THz beams. *Appl. Phys. Lett.* **69**, 1026 (1996).

[100] D. You and P. H. Bucksbaum. Propagation of half-cycle far-infrared pulses. *J. Opt. Soc. Am. B* **14**, 1651 (1997).

[101] D. You, R. R. Jones, P. H. Bucksbaum, and D. R. Dykaar. Generation of high-power sub-single-cycle 500fs e-m pulses. *Opt. Lett.* **18**, 290–292 (1993).

[102] G. Zhao, R. Schouten, N. v. d. Valk, W. Wenkenbach, and P. C. M. Planken. Design and performance of a THz emission and detection setup based on a semi-insulating GaAs emitter. *Rev. Sci. Instr.* **73**, 1715 (2002).

[103] J. Zhou, J. Peatross, M. M. Murnane, H. C. Kapteyn, and I. P. Christov. Enhanced high-harmonic generation using 25fs laser pulses. *Phys. Rev. Lett.* **76**, 752 (1996).

[104] M. L. Zimmerman, J .C. Castro, and D. Kleppner. Diamagnetic structure of Na Rydberg states. *Phys. Rev. Lett.* **40**, 1083 (1978).

[105] M. L. Zimmerman, M. G. Littman, M. M. Kash, and D. Kleppner. Stark structure of the Rydberg states of alkali-metal atoms. *Phys. Rev. A* **20**, 2251 (1979).

Summary

In this thesis we describe experiments on Rydberg atoms in electric fields with frequencies ranging from the radiofrequency domain until the terahertz region. Rydberg atoms are a peculiar kind of matter with properties that put them on the borderline between the worlds of classical and quantum mechanics. Rydberg atoms are atoms in a highly excited electronic state, which have one weakly bound electron orbiting around the atomic core on a trajectory governed by the Kepler laws, an ellipse. In chapter 1, we describe the basic concepts of Rydberg atom physics. We show results from a semi-classical model of Rydberg atoms and discuss the conclusions which can be drawn from that model. As an example, we present results on the ionization of Rydberg states in an external magnetic field by ultrashort half-cycle THz pulses.

Electromagnetic pulses are frequently characterized by their amplitude, duration, and carrier frequency. For pulses with a duration in the order of the cycle time of the carrier frequency, the phase between the carrier frequency and the pulse envelope becomes important. For pulses containing only a few cycles of the field, the carrier-envelope (CE) phase ϕ determines the symmetry of the field: $\phi = 0$ (sine) pulses are point symmetric, $\phi = \pi/2$ (cosine) pulses are mirror symmetric.

In the optical domain, generation of ultrashort (4-8 fs) laser pulses with a controlled CE phase is extremely difficult and has been achieved only very recently. In the radiofrequency (RF) domain, continuous control over all pulse parameters is readily achieved. In chapter 2, we present time-resolved measurements of the electron emission of rubidium Rydberg atoms ionized by few-cycle RF pulses with sub-cycle time resolution. The electron emission occurs in bursts with remixing of Stark states by the Rb core as the mechanism responsible for this intermittent ionization. We show measurements of the influence of amplitude, pulse duration and CE phase on the temporal ionization profile and discuss implications of our work as a model system for high-order harmonic generation and the production of single attosecond pulses, two research fields which have gained enormous momentum in the last few years.

In chapter 3 we investigate the asymmetry in the direction of emission in the ionization of Rydberg atoms by few-cycle RF pulses. The ejection direction strongly depends on the pulse amplitude, duration and CE phase. For short low-amplitude pulses we find the expected results: symmetric emission for symmetric (sine) pulses, asymmetric emission for asymmetric (cosine) pulses. As the pulse duration increases, the asymmetry disappears. For strong

pulses, the emission direction is dominated by depletion at the onset of the pulse and is much more complex. The asymmetry is not related to the symmetry of the field in this case and persists up to much longer pulse durations. These results have predictive power for the physics of atoms in ultrashort intense laser fields and show the implications of depletion.

State-selective field ionization (SFI), time-resolved measurement of the ionization of Rydberg states by slowly ramped fields, is a widely employed technique in Rydberg atom experiments. Unfortunately, spin-orbit effects make the selectivity of the SFI process dependent on the atomic core and lead to a much lesser resolution in heavy atoms such as rubidium. Rubidium, on the other hand, offers considerable experimental advantages, such as the low melting point and high vapor pressure and the fact that the Rydberg states can be excited using only one dye laser at a convenient wavelength. In chapter 4 we investigate the effect of carefully chosen field ramp combinations on the selectivity of SFI in Rb. For ramps constructed from a fast step and a slow ramp, we find a much higher selectivity of SFI in Rb, which allows us to employ a fitting procedure to extract the state composition from an unknown mixture of states.

In the electromagnetic spectrum, the wavelength region between microwaves and the infrared, the so-called far-infrared or THz region, is difficult to access since the frequencies are too high for electronics and too low for optical methods. One way to generate radiation in this this wavelength region is by exciting ultrashort transients in a biased semiconductor wafer, which radiate ultrashort pulses with a spectrum ranging from a few GHz to around 2 THz. These pulses which have a temporal shape of half an optical cycle, therefore they are often called half-cycle pulses. Because of the nonionizing character and the short wavelength of these pulses they are considered a promising tool in medical imaging as well as material probing applications. In chapter 5 we make use of the small binding energy of Rydberg atoms in an electric field to make a twodimensional photocathode for THz radiation. We show images of a cross-shaped mask as well as the unfocussed THz beam profile. In contrast to existing THz imaging techniques, the Rydberg atom photocathode is not restricted to coherent radiation and does not require the temporal overlap of two ultrashort pulses.

In chapter 6 we demonstrate an intricate combination of strong and weak interactions of a THz half-cycle pulse with Rydberg atoms which leads to the interesting situation that a transition which is resonant with a frequency that was taken out of the frequency spectrum is enhanced. In the experiment, a terahertz (THz) pulse propagates through water vapor, which absorbs on discrete lines in the THz spectrum. The resulting pulse interacts with a Rydberg atom which has a resonant transition with a water absorption line. If the half-cycle pulse is strong enough to induce a nonlinear interaction, the transition probability is enhanced rather than decreased although this frequency was taken out of the spectrum by the water vapor. This effect is applied to determine the position and width of a rotational line in gaseous water.

Samenvatting

Dit proefschrift draait om Rydbergatomen in oscillerende elektrische velden met zeer uiteenlopende frequenties van megahertz tot terahertz. Rydbergatomen zijn een heel speciale vorm van materie, omdat ze eigenschappen bezitten die ze op de grens tussen klassieke en quantummechanica plaatsen. Rydbergatomen zijn atomen in een hoog aangeslagen toestand met één heel zwak gebonden elektron dat in een baan om de rest van het atoom draait. In de klassieke mechanica wordt deze baan door de wetten van Kepler beschreven. In hoofdstuk 1 beschrijven wij de fundamentele eigenschappen van Rydbergatomen. Wij tonen resultaten van een semi-klassieke simulatie van Rydbergatomen en bespreken de conclusies die daaruit volgen. Als voorbeeld gebruiken wij Rydbergatomen in een sterk magnetisch veld, die geïoniseerd worden door ultrakorte pulsen die uit een halve golf bestaan.

Elektromagnetische pulsen worden vaak gekarakteriseerd door middel van hun amplitude, tijdsduur en frequentie. Voor pulsen met een tijdsduur die in de buurt komt van de oscillatietijd van de draaggolf, begint de fase van de draaggolf ten opzichte van de omhullende van de puls een belangrijke rol te spelen. Voor pulsen die maar weinige oscillaties van het veld bevatten bepaalt die fase de symmetrie van het veld: $\phi = 0$ (sinus) pulsen zijn puntsymmetrisch, $\phi = \pi/2$ (cosinus) pulsen zijn spiegelsymmetrisch.

In het optische domein is het maken van ultrakorte (4-8 fs) laserpulsen met een gestabiliseerde fase extreem moeilijk en dit is dan ook pas kort geleden gelukt. In het radiofrequentie domein is het bepalen van alle pulsparameters relatief gemakkelijk. In hoofdstuk 2 laten wij tijdopgeloste metingen zien van de elektronenemissie van rubidium Rydbergatomen die geïoniseerd zijn door radiofrequentie pulsen die uit slechts een gering aantal oscillaties bestaan. De elektronenemissie gebeurt in uitbarstingen, waarbij een hermenging van Starktoestanden door de Rb kern verantwoordelijk is voor deze gepulste emissie. Wij tonen metingen die de invloed van amplitude, pulsduur en fase op de tijdafhankelijke emissie laten zien. Tevens bespreken wij de relevantie als modelsysteem voor hoge harmonische generatie en de productie van attoseconden-pulsen, twee gebieden die in de laatste jaren enorm gegroeid zijn.

In hoofdstuk 3 onderzoeken wij de asymmetrie in de richting waarin de elektronen uitgezonden worden. Deze richting is sterk afhankelijk van de pulsamplitude, pulsduur en fase. Voor korte pulsen met lage amplitudes vinden wij de verwachte resultaten: symmetrische emissie voor puntsymmetrische (sinus) pulsen, asymmetrische emissie voor spiegelsymmetrische (cosinus) pulsen. Met langer wordende pulsduur verdwijnt de asymmetrie. Echter, voor

sterke pulsen wordt de emissierichting bepaald door depletie tijdens het begin van de puls en vertoont het emissierichting een veel complexer gedrag. De asymmetrie is in dit geval niet afhankelijk van de symmetrie van het veld en blijft tot veel langere pulsduren bestaan. Deze resultaten kunnen voorspellingen opleveren voor de fysica van atomen in ultrakorte sterke laservelden en ze laten de invloed van depletie zien.

Selectieve veldionisatie (state-selective field ionization, SFI), dat wil zeggen tijdopgeloste meting van de ionisatie van Rydbergtoestanden door langzaam groter wordende elektrische velden, is een vaak gebruikte techniek in experimenten met Rydbergatomen. Helaas hangt de selectiviteit van dit proces af van het atoom dat gebruikt wordt want spin-baan effecten maken selectieve veldionisatie minder selectief voor zwaardere atomen zoals rubidium. Rubidium heeft echter grote experimentele voordelen vanwege zijn lage smeltpunt en hoge dampdruk en het feit dat Rydbergtoestanden aangeslagen kunnen worden met behulp van slechts één kleurstoflaser bij een eenvoudig te genereren golflengte. In hoofdstuk 4 onderzoeken wij de invloed van de vorm van het elektrische veld. Voor veldvormen die uit een snelle stap en vervolgens een langzame stijging bestaan, wordt de selectiviteit van het selectieve veldionisatieproces verhoogd. Dit maakt het mogelijk om een fit toe te passen om de samenstelling van een onbekend mengsel van toestanden te bepalen.

In het electromagnetische spectrum zijn frequenties tussen het microgolfgebied en het verre infrarood, het zogenaamde THz-gebied, heel moeilijk op te wekken, omdat deze frequenties te hoog zijn voor elektronische en te laag voor optische methodes. Een manier om deze frequenties op te wekken is door een halfgeleider die onder hoogspanning staat te beschieten met een ultrakorte laserpuls. Daardoor worden elektronen in de geleidingsband gebracht en door de hoogspanning versneld. De versnelde ladingsdragers zenden een korte elektromagnetische puls uit met frequenties tussen enkele GHz en 2 THz. Die pulsen hebben de vorm van een halve golf, vandaar dat ze ook “half-cycle pulsen” worden genoemd. Vanwege de korte golflengte en omdat het niet-ioniserende straling is, zijn dit soort pulsen interessant voor bijvoorbeeld medische niet-destructieve afbeeldingstoepassingen. In hoofdstuk 5 maken wij gebruik van de lage bindingsenergie van Rydbergatomen in een elektrisch veld om een twee-dimensionale fotokathode voor THz straling te maken. Wij laten beelden zien van een kruisvormig masker en van het bundelprofiel van de THz puls in het verre veld. De Rydbergatoom-photokathode heeft geen coherente straling nodig en het is niet vereist om twee ultrakorte pulsen in tijd te laten overlappen.

Hoofdstuk 6 gaat over een subtiele combinatie van sterke en zwakke interacties van THz halfgolfpulsen met Rydbergatomen, die tot de interessante situatie leidt dat een overgang met een frequentie die uit het pulsspectrum verwijderd is, juist waarschijnlijker wordt. In het experiment wordt een THz puls door waterdamp heen gestuurd. Het water absorbeert op discrete absorptielijnen in het THz spectrum. De puls die overblijft wisselwerkt met een Rydbergatoom, dat een overgang heeft die resonant is met een geabsorbeerde frequentie. Als de halfgolfpuls sterk genoeg is om een niet-lineair gedrag te veroorzaken, wordt de overgang waarschijnlijker in plaats van onwaarschijnlijker als de overgangsfrequentie door de waterdamp uit het spectrum is verwijderd. Wij gebruiken dit effect om de positie en lijnbreedte van een rotationele absorptielijn in waterdamp te bepalen.

Acknowledgments

It is impossible to list all the people who contribute to a thesis. Here I only name a small subset, which can not be complete.

I want to thank my promoter Wim van der Zande for taking me and my project over with great enthusiasm. I very much appreciate his openness to new ideas and the freedom he gave me in my work while still guiding when necessary. I learned a lot from his way of connecting different fields of physics and different points of view.

From my copromotor Bart Noordam I learned not only about Rydberg atoms but also about a way of tackling problems which is focused on the outcome. I was always impressed by his ability to analyze a problem or situation and find the crux of the matter.

The other QDAMS group leaders were always willing to answer questions and discuss problems. Harm Geert Muller, Mark Vrakking and Huib Bakker, thanks for that.

I also profited from visitors in our group. Charlie Conover introduced me to the calculation of Zeeman and Stark maps which I made heavy use of, from Francis Robicheaux I learned a lot about many aspects of Rydberg atoms.

Much of the joy and success of any type of work depends on the people around. With Marcel Warntjes I had a good time in the lab and afterwards and he and Kees Wesdorp were always in for an espresso and a chat. The discussions and experiments with them taught me a lot about Rydberg atoms. My roommates Anouk Wetzels and Afric Meyer not only made the atmosphere in and out of office fun, but also contributed to the success of this thesis in many ways. Later when I shared the room with Ben Veihelmann and Laura Dinu, they endured my phd-endtime mood and still could stand me for dinners and all kind of fun stuff after work. Rüdiger Lang, Annemieke Petrignani, Hester Volten and Jason Williams made coffee breaks and lunch club meetings always enjoyable and helped in many ways. Thank you all.

This thesis would have been absolutely impossible without the help of the technical staff of AMOLF. Hinco Schoenmaker just made things work. Rob Kemper always knows what to do or whom to ask. Thanks a lot. The people from E&I did great work, Duncan Verheijde solved problems even before being asked, Idzart Attema, Anton Vijftigschild and Hans ter Horst always came up with bright solutions. Anton Buijserd kept the lasers running, even after serious floodings. Hartstikke bedankt.

The administration of AMOLF was a big help. The word “problem” seems to be known there only in combination with “no”. No matter if a meeting has to be organized, a conference

booked and payed or contract extended, the guys from the financial and personell department, the secretariate and the library just do it. Thanks for the complete lack of bureaucracy, which is truly remarkable. Roudy van der Wijk helped a lot with finding houses, no small thing in Amsterdam.

Less beer would have been consumed, less glasses destroyed and less pigs eaten without Rich, Cendrine and Andrea. Thanks for the friendship and the good times.

Zum Schluß will ich ganz besonders meinen Eltern und meiner Familie, meiner Schwester und meinem Bruder sowie meiner Tante und meinem Onkel danken. Sie haben mich immer mit unglaublicher Großzügigkeit mit Unterstützung, Energie und Essenspaketen versorgt. Herzlichen Dank dafür.